# The ORP9-ORP11 dimer promotes sphingomyelin synthesis

**Authors:**

*Birol Cabukusta[1,§], Shalom Borst Pauwels[1], Jimmy J.L.L. Akkermans[1], Niek Blomberg[2], Aat A. Mulder[3], Roman I. Koning[3], Martin Giera[2] and Jacques Neefjes[1]*

*[1]Cell and Chemical Biology, Oncode Institute, Leiden University Medical Center, Leiden, Netherlands*
*[2] Centre for Proteomics and Metabolomics, Leiden University Medical Center, Leiden, Netherlands*
*[3] Electron Microscopy Facility, Cell and Chemical Biology, Leiden University Medical Center, Leiden, Netherlands*

*[§]Correspondence to b.cabukusta@lumc.nl*

**Abstract**

Numerous lipids are heterogeneously distributed among organelles. Most lipid trafficking between organelles is achieved by a group of lipid transfer proteins (LTPs) that carry lipids using their hydrophobic cavities. The human genome encodes many intracellular LTPs responsible for lipid trafficking and the function of many LTPs in defining cellular lipid levels and distributions is unclear. Here, we created a gene knockout library targeting 90 intracellular LTPs and performed whole-cell lipidomics analysis. This analysis confirmed known lipid disturbances and identified new ones caused by loss of LTPs. Among these, we found major sphingolipid imbalances in ORP9 and ORP11 knockout cells, two proteins of previously unknown function in sphingolipid metabolism. ORP9 and ORP11 form a heterodimer to localize at the ER-*trans* Golgi membrane contact sites, where the dimer exchanges phosphatidylserine (PS) for phosphatidylinositol-4-phosphate (PI(4)P) between the two organelles. Consequently, loss of either protein causes phospholipid imbalances in the Golgi apparatus that result in lowered sphingomyelin synthesis at this organelle. Overall, our LTP knockout library toolbox identifies various proteins in control of cellular lipid levels, including the ORP9-ORP11 heterodimer, which exchanges PS and PI(4)P at the ER-Golgi membrane contact site as a critical step in sphingomyelin synthesis in the Golgi apparatus.

## Introduction

Many types of lipids are heterogeneously distributed among various organelles of the cell[1]. Due to the hydrophobic nature of lipids, their trafficking needs to be facilitated. While vesicular trafficking transports lipids in bulk between organelles, non-vesicular trafficking of lipids also play a role in defining lipid compositions of organelles. In fact, many organelles that do not receive any vesicular cargo rely on this route. Non-vesicular trafficking of lipids is achieved by a group of lipid transfer proteins (LTPs) that carry lipids using their hydrophobic cavities to stabilize lipids in the aqueous intracellular environment[2]. LTPs often contain targeting domains, motifs, transmembrane regions, amphipathic helices or surface charge to define their donor and acceptor organelles[3]. Many LTPs localize at two organelles simultaneously at membrane contact sites, where these organelles come closer to exchange information and material, including lipids[4,5].

The human genome encodes over 150 LTPs; new LTPs and LTP families are being characterized every so often[2,6–13]. About 50 of these proteins are secreted and are involved in carrying lipids, metals, lipopolysaccharides, and other small molecules in blood plasma[2]. The remaining intracellular LTPs are mainly responsible for intracellular lipid trafficking among organelles. Since many lipid-modifying enzymes are localized to different organelles, LTPs also feed metabolic lipid fluxes, eventually defining cellular lipid levels[14]. For example, LTP-mediated trafficking of ceramide from the endoplasmic reticulum (ER) to the *trans* Golgi is needed for sphingomyelin synthesis[15]. While achieving a considerable understanding of some LTPs in the last years, the function of many LTPs in defining cellular levels and distributions remains unclear.

To study LTPs systematically, we designed and created an arrayed gene knockout library targeting 90 intracellular LTPs based on the CRISPR/Cas9 technology. Lipidomics analysis of the library-generated LTP knockout cells confirmed known and identified novel lipid disturbances emerging from loss of LTPs. These included CERT, GLTP, NPC1 and NPC2 knockout cells with altered sphingolipid levels. Furthermore, we

identified major sphingolipid imbalances in ORP9 and ORP11 knockout cells, two proteins of unknown function in sphingolipid metabolism. ORP9 and ORP11 form a heterodimer to localize at the ER-*trans* Golgi membrane contact sites. At this contact site, the ORP9-ORP11 dimer transfers phosphatidylserine (PS) from the ER to the Golgi and phosphatidylinositol-4-phosphate (PI(4)P) in the opposite direction. Consequently, loss of either protein causes phospholipid imbalances in the Golgi apparatus that results in lowered sphingomyelin synthesis capacity at this organelle. Collectively, our LTP knockout library toolbox identified various proteins controlling cellular lipid levels. Among these, we found the ORP9-ORP11 heterodimer defining phospholipid composition of the *trans* Golgi as a critical step in sphingomyelin synthesis. These findings highlighted that phospholipid and sphingolipid gradients along the secretory pathway are linked at the ER-Golgi membrane contact sites.

## Results

### 1) A CRISPR knockout library targeting lipid transfer proteins

To understand the function of LTPs in defining cellular levels and distributions, we created an arrayed CRISPR/Cas9 knockout library targeting LTPs. We targeted only the intracellular LTPs in the library and excluded extracellular proteins, such as LIPOCALIN and LBP-BPI-CETP families[2]. In this library, 90 wells of a 96-well plate were used for targeting LTPs and 6 for non-targeting (NT) controls (Fig. 1A). For optimal gene disruption, we used a lentiviral gene delivery system and 3 guide RNAs per gene – a method also used by others to increase the frequency of gene disruption[16]. We applied the LTP knockout library to MelJuSo, a human melanoma cell line. The efficiency of the knockout strategy was confirmed by western blotting of selected wells (Fig. 1B).

Next, we performed whole-cell lipidomics analysis of the LTP knockout cells. To this end, library-generated MelJuSo cells were grown in lipid-depleted serum and analysed using a lipidomics platform detecting 17 different lipid classes thrice on average (Fig. 1A). One of the detected lipid classes, hexosylceramide, can correspond to glucosylceramide and galactosylceramide – two isomeric lipids in mammalian cells. By metabolic chasing of a fluorescent ceramide analogue in cells silenced for glucosylceramide synthase or galactosylceramide synthase; or treated with the glucosylceramide synthase inhibitor PDMP, we validated that glucosylceramide is the major hexosylceramide in MelJuSo cells (Fig. S1). This further substantiated the previous reports of galactosylceramide being present mainly in oligodendrocytes[17].

We next calculated the z-scores within each lipid class based on their relative abundance per measurement and plotted their average for LTP knockout cell lines. The analysis revealed many LTP knockout cells with lipid imbalances (Fig. 1C, Fig. S2A). Meanwhile, no z-score above the absolute value of 2 was observed for NT control cells (Fig. S2B). Overall, the lipidomics analysis of the LTP knockout library uncovered numerous candidate regulators of cellular lipid levels.

### 2) NPC1 and NPC2 knockout cells accumulate sphingomyelin in lysosomes and the plasma membrane

Lipidomics analysis of the LTP knockout library revealed various anticipated imbalances. Among these candidate regulators of cellular lipid levels, those related to sphingolipid metabolism are notable. This is

likely due to many enzymatic steps of sphingolipid metabolism being more linear and lacking the elasticity of phospholipids[1,14]. In the analysis, we identified GLTP knockout cells with lowered glucosylceramide levels (Fig. 2A, Fig. S3A-C). Loss of GLTP is recently reported to block ER-to-Golgi anterograde vesicular trafficking that results in lowered glucosylceramide synthesis[18].

In addition, we observed NPC1 and NPC2 knockout cells with elevated sphingolipid levels (Fig. 1B). Mutations in *NPC1* and *NPC2* genes are the cause of Niemann-Pick disease, type C that leads to lysosomal accumulation of cholesterol[19]. Cells lacking NPC1 or NPC2 function also accumulate sphingolipids[20]. Our observation of elevated sphingolipid levels in NPC1 and NPC2 knockout cells was present in all sphingolipid classes (Fig. 2B, C). Meanwhile phospholipid levels were not altered dramatically in these cells (Fig. S3D). To confirm whether this increase is associated with lysosomal accumulation of sphingolipids, we used a sphingomyelin-binding biosensor based on the equinatoxin secreted by the beadlet anemone *Actinia equina* (Fig. S3E)[21,22]. Immunofluorescence staining of NPC1 and NPC2 knockout cells using the biosensor showed lysosomal accumulation of sphingomyelin (Fig. 2D). Flow cytometry analysis using the sphingomyelin biosensor and the GM1 glycosphingolipid biosensor, the B subunit of cholera toxin, demonstrated that sphingolipid accumulation is also reflected on the cell surface of NPC1 and NPC2 knockouts (Fig. 2E, F). Meanwhile, the surface protein levels were not altered as detected by staining for the tetraspanin protein CD63. Collectively, our results corroborate the sphingolipid accumulation in NPC1 and NPC2 deficient cells and illustrate that the LTP knockout library is a viable tool to study LTPs and their role in regulating cellular lipid levels.

**3) CERT, ORP9 and ORP11 knockout cells demonstrate reduced sphingomyelin levels**

Sphingomyelin is the major sphingolipid in mammalian cells, and it is mainly synthesized in the *trans* Golgi from ceramide delivered from the ER. The non-vesicular trafficking of ceramide from the ER to the *trans* Golgi is mediated by the ceramide transfer protein CERT[15,23] (Fig. 3B). Our analysis identified CERT knockouts with the lowest sphingomyelin levels (Fig. 1C, 3A). These cells also demonstrate increased glucosylceramide levels, likely as a compensation mechanism (Fig. 3A). Furthermore, we found decreased sphingomyelin and increased glucosylceramide levels in ORP9 and ORP11 knockout cells – two proteins of unknown role in sphingolipid metabolism (Fig. 1C, 3A). The sphingolipid imbalances in all three knockout cells –CERT, ORP9, and ORP11– were also represented in many sphingolipid subspecies (Fig. 3C, Fig. S4B). Lowered sphingomyelin levels of the three knockout cells were further confirmed by their sensitivity towards methyl-β-cyclodextrin treatment (Fig. 3D). Meanwhile, none of the three knockout cells demonstrated phospholipid imbalances to a compelling degree (Fig. S4A).

The observation that ORP9 and ORP11 knockout cells mimic CERT knockouts implied a role for ORP9 and ORP11 in *de novo* sphingomyelin synthesis, whereas loss of neither ORP9 nor ORP11 reduced CERT protein levels (Fig. 3E). ORP9 and ORP11 each contain a PH domain mediating localization at the *trans* Golgi, the site of *de novo* sphingomyelin synthesis (Fig.3F, G). As loss of either ORP9 or ORP11 did not alter the Golgi ultrastructure as detected by light or electron microscopy (Fig. S5), it further suggested that ORP9 and ORP11 affect sphingomyelin levels by a previously unknown mechanism. Next, we investigated the possible mechanism by which ORP9 and ORP11 regulate cellular sphingolipid levels.

125 **4) Dimerization is critical for the ER-Golgi contact site localization of ORP9 and ORP11**

126 ORP9 and ORP11 interact with each other via their regions between their PH and ORD domains[24]. As no
127 other domain is found in this region, we speculated some secondary structures must facilitate the
128 dimerization. AlphaFold and PCOILS coiled coils prediction tool suggested that ORP9 and ORP11 contain
129 two alpha helices each in this region – hereafter referred as "*coils*" (Fig. 4A, S6A, B). AlphaFold-Multimer
130 suggested that the coils of ORP9 and ORP11 interact with each other (Fig. 4B, S6C-D). Identical analysis
131 of the full-length proteins predicted that the coils drive dimerization of the two proteins (Fig. 4C, D, S6E).
132 This was tested by targeting the coils of ORP9 to the mitochondrial outer membrane using the *N*-terminal
133 sequence of TOM70. In cells expressing mitochondria-targeted ORP9 coils, the coils of ORP11 located to
134 this organelle (Fig. 4C, D). The absence of either coil prevented the colocalization, suggesting that the coils
135 of ORP9 and ORP11 are sufficient for their dimerization. This finding was validated by co-
136 immunoprecipitations (Fig. 4E).
137
138 ORP9, but not ORP11, contains a FFAT, two phenylalanines in an acidic tract, motif that drives ER
139 localization by interacting with the ER-resident VAPA and VAPB[25]. Despite not containing a FFAT motif,
140 ORP11 could interact with VAPA and VAPB by its dimerization with ORP9. We tested this by co-
141 immunoprecipitations, where ORP11 could be co-isolated with VAPA from cells expressing VAPA, ORP9
142 and ORP11 (Fig. 4J). This interaction was diminished significantly when ORP9 was not co-expressed.
143 Furthermore, a VAPA mutant unable to interact with FFAT motifs failed to interact with either ORP9 or
144 ORP11, showing that ORP11 interacts with VAPA indirectly via the ORP9-FFAT motif.
145
146 We and others previously showed that in addition to VAPA and VAPB, the human proteome contains three
147 other proteins interacting with FFAT and related short linear motifs: MOSPD1, MOSPD2 and MOSPD3[26,27].
148 In our earlier efforts to identify interaction partners of VAPA, VAPB and other motif-binding proteins, we
149 performed BioID, proximity biotinylation followed by proteomics, identification of membrane contact sites
150 proteins[27]. In this analysis, ORP9 and ORP11 were found in proximity with VAPA and VAPB but not with
151 other motif-binding proteins (Fig. S6F). This further confirmed that despite lacking a FFAT motif, ORP11
152 together with ORP9 is part of VAPA- and VAPB-mediated membrane contact sites.
153
154 The Golgi localization of ORP9 and ORP11 is mediated by their PH domain interacting with
155 phosphatidylinositol phosphates[24]. We observed that the PH domains of ORP9 and ORP11 localized only
156 partially to the Golgi and demonstrated strong cytoplasmic localization, unlike the PH domains of OSBP
157 and CERT that show exclusive localization to this organelle[28,29] (Fig. 4H, S7D). We hypothesized that the
158 dimerization of ORP9 and ORP11 is a mechanism to increase their avidity towards *trans* Golgi membranes.
159 To test this, we created a chimera containing ORP9- and ORP11-PH domains that localized to the Golgi
160 more efficiently than the individual PH domains (Fig. 4H, I). This also implied that loss of either protein
161 should reduce the other's localization to the *trans* Golgi. Immunofluorescence staining of ORP9 and ORP11
162 knockout cells for the same proteins confirmed that both ORP9 and ORP11 are required for the Golgi
163 localization of the other protein (Fig. 5). Meanwhile, loss of either protein did not influence the levels of the
164 other (Fig. 3E). Our results collectively show that the dimerization of ORP9 and ORP11 via their coils is
165 required for the localization of ORP9-ORP11 dimer to the ER and the *trans* Golgi simultaneously.
166

167 **5) ORP9 and ORP11 are essential for PS and PI(4)P levels in the Golgi apparatus**

168 ORP9 and ORP11 belong to the OSBP-related protein (ORP) family that transfers sterols or PS while
169 transferring phosphatidylinositol phosphates in the opposite direction[30–33] (Fig. 6A, S7B). ORP9 and ORP11
170 carry the conserved PS binding site and are recently shown to relocate to the site of lysosomal damage to
171 supply PS for membrane repair[34]. Using an *in vitro* lipid transfer assay, we confirmed that the lipid transfer
172 domains (ORD) of ORP9 and ORP11 are sufficient to traffic PS *in vitro* (Fig. 6B, C). ORP9 and ORP10, but
173 not ORP11, are shown to traffic PI(4)P[35,36]. Using a PI(4)P transfer assay that utilizes the PI(4)P-binding
174 PH domain of FAPP1, we show that ORD of ORP11 can also traffic PI(4)P between model membranes
175 (Fig. 6D, E, S7C, D)[37]. Furthermore, similar to ORP5, ORP8 and ORP10, the PS-trafficking activity of
176 ORP9- and ORP11-ORDs was improved when acceptor liposomes were decorated with PI(4)P[35,38,39] (Fig.
177 S7E). This indicated that ORDs of ORP9 and ORP11 transport PI(4)P in the opposite direction of PS
178 trafficking.
179
180 To demonstrate the contribution of ORP9-ORP11 dimerization to their lipid transfer ability at membrane
181 contact sites, we reconstituted these sites *in vitro* by attaching a His-tagged VAPB devoid of its
182 transmembrane helix to donor liposomes and providing full-length ORP9 and ORP11 as tethers to the
183 acceptor liposomes (Fig. 6F, S7F-H). PS transfer assay in these reconstituted contact sites showed that as
184 a trimer, the ORP9-ORP11-VAPB complex displays an improved lipid transfer capacity (Fig. 6G, H).
185
186 PS is synthesized in the ER and its concentration increases along the secretory pathway as it is enriched
187 on the cytosolic leaflet of the plasma membrane[14]. PI(4)P, on the other hand, is abundant in the *trans* Golgi,
188 where it recruits many proteins to this membrane[40]. Another LTP localized at the ER-*trans* Golgi membrane
189 contact sites, OSBP transfers cholesterol from the ER to the *trans* Golgi, while counter transporting PI(4)P
190 to the ER for its hydrolysis by the ER-resident PI(4)P phosphatase SAC1 (Fig. 8). Homologous to OSBP,
191 the ORP9-ORP11 dimer resides in the ideal intracellular interface to traffic PS in anterograde and PI(4)P
192 in retrograde direction between the ER and *trans* Golgi (Fig. 8). This also suggested that the loss of either
193 protein would cause PS and PI(4)P imbalances between the ER and *trans* Golgi. We tested this notion by
194 using PI(4)P- and PS-binding biosensors[41,42] (Fig. S7I, J). Golgi localization of these sensors indicated that
195 PS levels were decreased in the Golgi of these cells (Fig. 6I, J). Also, PI(4)P showed accumulation in the
196 Golgi of ORP9 and ORP11 knockout cells (Fig. 6K, L). We confirmed the PI(4)P accumulation by quantifying
197 the Golgi localization of a PI(4)P specific antibody (Fig. S7J). Interestingly, both phenotypes, lowered PS
198 and increased PI(4)P levels, were better pronounced in ORP9 knockout cells compared to ORP11
199 knockouts. Furthermore, both phenotypes could be rescued by reconstitution of the missing protein (Fig.
200 6J, L). Overall, these findings suggested that the ORP9-ORP11 dimer is required for maintaining PS and
201 reducing PI(4)P levels in the Golgi apparatus.
202
203 **6) *De novo* sphingomyelin synthesis in the Golgi is impaired in ORP9 and ORP11 knockouts**

204 Next, we set out to investigate the possible role of ORP9 and ORP11 in regulating cellular sphingomyelin
205 levels. By performing a sphingomyelin synthase activity assay that uses the fluorescent ceramide analogue
206 NBD-ceramide as a substrate[43], we found that ORP9 and ORP11 knockout cells do not have reduced
207 sphingomyelin synthesis capacity (Fig. 7A, B). The same was also found in CERT knockout cells. Whereas

all three knockouts demonstrated increased glucosylceramide synthesis capacity, supporting the lipidomics analysis (Fig. 3A). Unaltered sphingomyelin synthesis capacity was further validated by the unreduced protein and mRNA levels of both human sphingomyelin synthases, SMS1 and SMS2 (Fig. S8A, B).

SMS1 is localized at the *trans* Golgi, while SMS2 mainly localizes at the plasma membrane but is also found at the *trans* Golgi[44]. As the enzymatic activity assay in lysates reports on the global sphingomyelin synthesis capacity, we next investigated *de novo* sphingomyelin synthesis that occurs at the *trans* Golgi, where CERT as well as the ORP9-ORP11 dimer localize. For this purpose, we chased the metabolic fate of palmitic acid alkyne (Fig. 7C). Palmitic acid is the precursor of sphinganine and all sphingolipids (Fig. 3B, 7C). To enter the sphingolipid pathway, palmitic acid first needs to travel to the ER and later to the Golgi for conversion to sphingomyelin, unlike ceramide analogues, such as NBD-ceramide, that can be converted to sphingomyelin by the plasma membrane-resident SMS2. Furthermore, the palmitic acid alkyne does not contain a bulky fluorescent group and the terminal alkyne allows visualization by click chemistry (Fig. 7C). As this method enabled us to monitor *de novo* sphingomyelin production in intact cells, we confirmed the reduced *de novo* sphingomyelin synthesis in CERT knockout cells using this method (Fig. 7D, E, S8C). In addition, ORP9 and ORP11 knockouts also showed decreased conversion of palmitic acid to sphingomyelin, suggesting a similar defect as CERT knockouts. To confirm the decreased sphingomyelin synthesis, we quantified the Golgi localization of a DAG biosensor, C1ab domain of protein kinase D1, that can report on sphingomyelin synthesis[45,46]. This showed decreased DAG levels in the Golgi that can be accounted for lowered sphingomyelin synthesis (Fig. S8D).

The observations that loss of ORP9 or ORP11 does not affect CERT protein (Fig. 3E) or reduce CERT localization to the Golgi (Fig. S9) implied that CERT-mediated transfer routes are not affected in ORP9 or ORP11 knockouts. Lipidomics analysis showing accumulation of ceramide and glucosylceramide in ORP9/ORP11 knockouts further suggested the conversion of ER-bound ceramides to sphingomyelin in the Golgi is hampered.

To distinguish between two possibilities that may result in lowered sphingomyelin levels – a ceramide delivery defect to the *trans* Golgi or an inability to convert ceramide to sphingomyelin in the Golgi, we established an immunoisolation protocol for *trans* Golgi membranes using a monoclonal antibody against the *trans* Golgi marker Golgin-97 (Fig. 7F). These isolates were enriched for the *trans* Golgi marker Golgin-97 and were devoid of other organelle markers, such as the ER, mitochondria, and lysosomes (Fig. 7G). We confirmed the membrane integrity of Golgin-97-enriched fractions by their sphingomyelin synthase activity, as these multi-pass transmembrane proteins require intact membranes for activity[44] (Fig. S10A). Lipidomics analysis of these fractions validated that the loss of ORP11 and especially that of ORP9 results in lowered PS levels in the *trans* Golgi (Fig. 7H, S10B-D). The *trans* Golgi fractions also showed reduced sphingomyelin levels, confirming the limited *de novo* sphingomyelin synthesis (Fig. 7D, E, I S10E). Moreover, the same fractions showed elevated ceramide levels in these fractions (Fig. 7J, S10F), revealing that the knockouts do not have a ceramide delivery defect, but instead a lowered capacity to convert ceramide to sphingomyelin in their *trans* Golgi membranes. We tested this notion by performing a sphingomyelin synthase activity assay in the isolated Golgi membranes, where supplying excess substrate to these membranes bypasses the ceramide delivery routes (Fig. 7K, L). This assay further substantiated

that the Golgi of ORP11 and especially of ORP9 knockout cells have a lowered sphingomyelin synthesis capacity. Meanwhile, localization of both sphingomyelin synthases was not reduced in the Golgi, as detected by three different antibodies (Fig. S11). Collectively, our results indicate that PS-PI(4)P exchange between the ER and *trans* Golgi mediated by the ORP9-ORP11 LTP complex is critical for *de novo* sphingomyelin synthesis in *trans* Golgi.

## Discussion

In this study, we describe a gene knockout library for systematic characterization of intracellular LTPs. The arrayed design of the library enables high and low throughput analysis. As new LTPs are identified in regular basis, the arrayed feature of the library allows expansion to include newly identified LTPs, e.g. ATG2A, SHIP164, KIAA0100 (Hobbit in *Drosophila*), KIAA1109 (Csf1 in yeast) and RMDN3 are new human LTPs that are identified through the course of this study[8–10,12,13].

Lipidomics analysis of the library demonstrated many lipid imbalances. We further validated loss of NPC1, NPC2, CERT, and GLTP with sphingolipid imbalances[15,18,20] (Fig. 1C). In addition to sphingolipids imbalances, we found STARD7 knockout cells with increased levels of phosphatidylglycerol (PG), a lipid class exclusive to mitochondria in mammals (Fig. 1C). STARD7 is a phosphatidylcholine (PC) transfer protein that localizes to the mitochondrial intermembrane space to supply PC to the mitochondrial inner membrane[47–49]. Consequently, loss of STARD7 reduces PC levels in this membrane as well as decreasing cardiolipin levels and respiratory capacity[48,49]. While PC in the inner membrane is not a precursor of cardiolipin, it is possible the reduced PC levels in this membrane impair the activity of the cardiolipin synthase that uses PG as its substrate, suggesting an explanation for the PG accumulation in STARD7 knockout cells.

LTPs often localize at membrane contact sites to facilitate lipid exchanges between organelles. We found ORP9 and ORP11 localizing at the ER-*trans* Golgi contact sites to exchange PS and PI(4)P. We show that the dimerization is critical for the contact site localization, and consequently, loss of either protein is sufficient to disturb PS and PI(4)P levels in the Golgi. In return, this phospholipid imbalance reduces sphingomyelin synthesis capacity of the Golgi. Compared to ORP11 knockout cells, ORP9 knockout cells display more pronounced phenotypes of cellular sphingolipid imbalances (sphingomyelin and glucosylceramide), phospholipid imbalances in the Golgi apparatus (PS and PI(4)P), as well as reduced capacity of sphingomyelin synthesis in *trans* Golgi membranes. Furthermore, loss of ORP9 leads to a more dramatic effect on the Golgi localization of ORP11 than vice versa. This is most likely due to ORP9 providing a critical factor, i.e. the FFAT motif, for contact site localization, whereas it is possible the loss of ORP11 can be partially compensated by ORP10.

The contact site localization of the ORP9-ORP11 dimer is homologous to that of the ORP9-ORP10 dimer localizing at the ER-endosome and ER-Golgi contact sites asORP10 also uses its coiled coils to interact with ORP9[35,36]. In both LTP complexes, ORP9 provides the FFAT motif required for ER contact. ORP10 can also deliver PS to Golgi membranes[50], however, our lipidomics analysis of ORP10 knockout cells did not demonstrate any sphingolipid imbalances (Fig. S12A). Besides ORP9, ORP10 and ORP11, other LTPs are also shown to dimerize at the ER-Golgi interface. A recent structural study has revealed the architecture

of a previously-described OSBP dimerization that is mediated by a central core domain containing two alpha helices[51,52]. CERT forms a similar dimer and the conformational changes dictated by the central core domain is responsible for regulating the activity of the CERT dimer[53]. Both OSBP and CERT homodimers form a T-shaped structure, dissimilar to the heterodimers of ORP9, ORP10 and ORP11.

What distinguishes ORP11 from ORP10? An analysis of expression profiles from >900 cancer cell types showed that ORP10 and ORP11 are not differentially expressed (Fig. S12B). On the contrary, they show a positive correlation. It is possible that ORP9 interacts with ORP10 or ORP11 in different biological conditions or sub-cellular locations. ER-endosome contact site localization of the ORP9-ORP10 dimer supports this notion[35]. Even within the Golgi, ORP9-ORP10 and ORP9-ORP11 dimers might be facilitating lipid flows at different sub-organellar domains. The presence of multiple phosphatidylinositol (PI) transfer proteins localized at ER-*trans* Golgi contact sites feeding PI(4)P synthesis in the Golgi for distinct purposes and the observation of different PI(4)P-containing sub-domains in the Golgi promotes the idea that ORPs could localize at different Golgi sub-domains[55,56]. Furthermore, all three proteins, together with OSBP and ORP1L, are recruited to the lysosomal damage site in response to the increased PI(4)P levels on lysosomal delimiting membrane[34,57]. Collectively, these reports highlight the spatiotemporally dynamic nature of PI(4)P-mediated lipid trafficking and suggest that the two dimers could have different functions.

An intriguing observation is that the loss of ORP9 causes more accumulation of ceramide than CERT knockouts, despite loss of either protein leading to a comparable reduction of sphingomyelin levels. As the loss of CERT would lead to a ceramide accumulation in the ER, it is possible that such an accumulation in the ER is sensed to reduce ceramide production in this organelle. An ER-resident candidate ceramide sensor for this purpose was suggested previously[58]. Meanwhile, our findings show a ceramide accumulation in the *trans* Golgi of ORP9 knockouts. Accordingly, ceramide accumulation in the Golgi caused by the loss of ORP9 would fail to "*turn on*" an ER-localized ceramide sensing machinery, thus leading to further ceramide accumulation compared to CERT knockout cells. This notion also supports our finding that the loss of the ORP9-ORP11 dimer causes ceramide accumulation primarily in the Golgi.

Asymmetric distribution of lipids between two bilayer leaflets is a characteristic feature of the plasma membrane. This is owed to the build-up of sphingomyelin and cholesterol on the outer leaflet and PS on the inner leaflet[14]. The transition of the thin, symmetrical ER membrane to a thicker, rigid and asymmetrical one takes place in the Golgi (Fig. 8)[14]. Sphingolipid, cholesterol and PS concentrations also increase along the secretory pathway. Various mechanisms are described to drive the sphingolipid and cholesterol trafficking against the concentration gradient, including thermodynamic trapping of cholesterol due to complex formation with sphingomyelin or energy release from the retrograde trafficking of PI(4)P followed by its hydrolysis in the ER[14,31,59]. The same PI(4)P gradient between the ER and Golgi could also power the anterograde trafficking of PS, which, unlike sphingomyelin or cholesterol, is still exposed on the cytosolic leaflet of the Golgi where it has a higher concentration than the ER – thus, maintaining lipid trafficking against the gradient requires energy. In brief, our finding that the ORP9-ORP11-dimer-mediated phospholipid exchange promoting the sphingomyelin synthesis reveal further intertwining of lipid gradients along the secretory pathway at the ER-*trans* Golgi membrane contact sites.

**Conflict of Interest:**

Authors declare no conflict of interest.

**Acknowledgements:**

Authors thank Ruud Wijdeven, Robbert Q. Kim of LUMC protein facility, Carolina Jost and the members of the Neefjes lab for their technical and critical input. Authors are especially grateful to Joost Holthuis and Matthijs Kol of University of Osnabrück for their intellectual input.

342 **Materials and methods**

343

344 **Cell culture**

345 MelJuSo and HEK293T (ATCC CRL-3216) cells were cultured in IMDM (Gibco #21980) and DMEM (Gibco
346 #41966) supplemented with 8% fetal calf serum (Biowest #S1810), respectively. MelJuSo cell line
347 authentication was performed by Eurofins Genomics (19-ZE-000487).

348

349 **Library design, generation and transduction**

350 Targeting and non-targeting guide sequences (Supplementary Table 1) were obtained from the Brunello
351 Human CRISPR Knockout Pooled Library[60] and cloned into lentiCRISPR v2 plasmid[61] as described
352 previously[62]. Cloning of guide RNAs were individually confirmed by Sanger sequencing.

353

354 For library transduction, HEK cells were seeded on a 96-well plate on the day before transfection and
355 transfected with library plasmids and lentiviral packaging plasmids pRSVrev, pHCMV-G VSV-G, and
356 pMDLg/pRRE using polyethyleneimine (Polysciences #23966). A day after replacing the medium, virus was
357 harvested and MelJuSo cells were transduced in the presence of 4µg/ml polybrene (EMD Milipore #TR-
358 1003-G). Transduced cells were subjected to selection using 2µg/ml puromycin.

359

360 **Lipid extractions and lipidomics analysis**

361 For lipidomics analysis, library-generated cells were expanded to 15-cm dishes and cultured in IMDM
362 supplemented with lipid-depleted serum (Pel-Freez #37217-5) for 3-4 days. Next, cells were scraped in 2%
363 NaCl solution and lipids were extracted following the Bligh-Dyer protocol. In brief, harvested cells were
364 resuspended in 200µL 2% (w/v) NaCl followed by addition of 500µL methanol and 250µL chloroform.
365 Samples were vortexed for 5 min. Following phase separation by adding 250µL chloroform and 250µL
366 0.45% (w/v) NaCl, samples were centrifuged for 5min at 15,000xg. Next, bottom fractions were collected
367 and dried under continuous nitrogen stream.
368 Comprehensive, quantitative shotgun lipidomics was carried out as described in detail elsewhere[63,64].
369 Briefly, dried lipid extracts were spiked with 54 deuterated internal standards and dissolved in
370 methanol:chloroform 1:1 containing 10 mM ammonium acetate. Lipids are then analysed with a flow
371 injection method at a flow rate of 8 µL/min applying differential ion mobility for lipid class separation and
372 subsequent multiple reaction monitoring in positive and negative electrospray ionization mode. Using the
373 Shotgun Lipidomics Assistant (SLA) software individual lipid concentrations are calculated after correction
374 for their respective internal standards.

375

376 **Data analysis and statistics**

377

378 Data analyses, including lipidomics data analysis, were performed using R (4.1.0 "*Camp Pontanezen*") and
379 RStudio (2022.12.0+353) with following packages: *ggplot2*, *dplyr*, *readr*, *ggrepel*, *ggcorrplot2*, *reshape2*,
380 *ggbeeswarm*, *ggsignif*, *purr*, *tidyr*, and *tibble*. For Z-score calculations, first the percentages of each lipid
381 class within individual measurements were calculated, followed by calculating Z-scores for individual data
382 points using the following formula: "$Z = (x - \mu)/\sigma$", where $\mu$ is the mean percentage of a lipid class and $\sigma$ is

383 the standard deviation. Next, average Z-scores for LTP knockout cell lines were calculated. For POPC
384 normalized data analysis for the analysis of acyl chain distributions and Golgi lipidomics, each lipid
385 subspecies normalized to palmitoyl-oleoyl-phosphatidylcholine (POPC) levels. For Golgi lipidomics, POPC-
386 normalized values were normalized again to the mean of POPC-normalized values for MJS and gNT
387 samples. Raw lipidomics data available at Supplementary Table 2.
388
389 Mean values are denoted in all graphs except for boxplots. When present, error bars indicate standard
390 deviations. In boxplots, middle line denotes median, box boundaries denote the first (Q1) and third (Q3)
391 quartiles, and the lower and upper whiskers denote "*Q1-1.5*IQR"* and "*Q3+1.5*IQR*", respectively. IQR:
392 inter-quartile range. For statistical analysis, student's t-test is used, unless stated otherwise. *p<0.05,
393 **p<0.01, ***p<0.001, ****p<0.0001.
394
395 **Co-immunoprecipitation, SDS-PAGE and Western blotting**

396 Co-immunoprecipitation from HEK293T cells, SDS-PAGE and Western blotting were performed as
397 described previously[27].
398
399 **Immunofluorescence staining and quantifications**

400 For equinatoxin staining, cells were fixed with 4%PFA:PBS (v/v) and permeabilized with 10µg/ml digitonin
401 in PBS for 15min at RT. Further stainings were performed in PBS. PI4P staining was performed after fixation
402 in 2% PFA/PBS for 15 minutes followed by permeabilization with 20µM digitonin in Buffer A (20mM PIPES,
403 pH 6.8, 137mM NaCl and 2.7mM KCl). Blocking was performed in Buffer A supplemented with 5% (v/v)
404 serum. Next, cells were incubated with the PI(4)P antibody and the anti-mouse IgM secondary antibody,
405 respectively–both diluted in blocking solution. Cells were washed with buffer A and fixed in 2% PFA/PBS
406 for 5 minutes. Coverslips were mounted on slides using Vectashield Vibrance (Vector Laboratories #H-
407 1700).All other immunofluorescence staining was performed as described previously[27].
408
409 Images were acquired using a Zeiss LSM 900 with Airyscan. Images were analysed and quantified using
410 ImageJ/FIJI software. To quantify the Golgi localization of lipid biosensors (OSBP-PH, LactC2 and C1ab),
411 first a mask was created using Golgin-97 counter staining and this mask was used to quantify signal from
412 *trans* Golgi as well as the cytoplasm. Golgi localization of immunofluorescence staining of endogenous
413 proteins (ORP9, ORP11, CERT) and the PI(4)P antibody was performed first by creating a mask using
414 Golgin-97 and later using this mask to quantify signal of interest relative to signal of Golgin-97. Manders'
415 coefficient for colocalization was calculated using the Jacop plugin for ImageJ/FIJI.
416
417 **Flow cytometry analysis**

418 MelJuSo cells were brought to suspension by trypsinization and stained with the indicated probes on ice
419 prior to analysis using a BD LSR-II equipped with 488 and 561nm lasers. Data was analysed using FlowJo
420 v.10 software.
421
422 **Electron microscopy**

423 Cells cultured in 6-cm dishes were fixed for an hour at room temperature by adding double concentrated
424 fixative to the medium (final concentration: 1.5% glutaraldehyde in 0.1M cacodylate buffer). After three
425 times rinsing with 0.1 M cacodylate buffer, the cells were postfixed with 1% osmium tetroxide and 1.5%
426 uranyl acetate. Cells are dehydrated with a series of ethanol, followed by a series of mixtures of ethanol
427 and EPON (LX112, Leadd) and at the end pure EPON. BEEM capsules filed with EPON were placed on
428 the dishes with the open face down. After EPON polymerization at 40°C the first night and 70°C the second
429 night, the BEEM capsules were snapped off. Ultrathin sections 80 nm were made parallel to the surface of
430 the BEEM capsules containing the cultured cells. The sections were contrasted with uranyl acetate and
431 lead hydroxide and examined with a Tecnai Twin transmission electron microscope (Thermo Fisher,
432 Eindhoven, Netherlands). Overlapping images were automatically collected and stitched together into a
433 composite image as previously described[65].
434

435 **Recombinant protein expression and purification**

436 A codon optimized version of cDNA encoding the non-toxic version of equinatoxin[22] was ordered from IDT
437 technologies, GFP sequence was obtained from meGFP-C1 vector and a cDNA encoding the fusion protein
438 was synthesized using Gibson Assembly. A codon optimized version of cDNA encoding the PH domain of
439 FAPP1 containing the T13C, C37S, and C94Smutations were ordered from IDT technologies. cDNA
440 encoding human VAPB gene was described previously[27]. cDNAs encoding ORD domains of ORP9 and
441 ORP11, VAPB without its C-terminal transmembrane helix, FAPP1-PH, and EQT-GFP fusion protein were
442 cloned into a pNKI1.8/GST-expression vector.
443

444 For FAPP1-PH and VAPB-His expressions *E. coli* BL21 was grown in LB medium and expression was
445 induced when $OD_{600}$ was at 0.6 for overnight at 18ºC. For other proteins, *E. coli* BL21/Rosetta were grown
446 in 2xYT medium and expression was induced when $OD_{600}$ was at 1 for overnight at 18ºC. Bacterial pellets
447 were resuspended in GST purification buffer (50mM Tris pH 8.0, 250mM NaCl, 1mM EDTA, 1mM DTT)
448 and lysed by tip sonication. Lysates were cleared by centrifugation at 12,000xg for 30 min. Proteins were
449 purified using Glutathione Sepharose™ 4 Fast Flow (GE Healthcare #17-5132-03) and cleaved using 3C
450 protease protein prior to reverse purification using glutathione beads followed by a HiLoad 16/60 Superdex
451 75 size exclusion chromatography.
452

453 Full-length ORP9 and ORP11 were expressed using a baculovirus expression in *Spodoptera frugiperda*
454 (Sf9) using an adapted Bac-to-Bac system (Invitrogen). In brief, cDNAs were cloned to an in-house insect
455 expression vector and bacmids were generated using EmBacY cells (Geneva Biotech) isolated using
456 isopropanol precipitation. 10 µg Bcmid was transfected to sedentary Sf9 cells using CellFectin (Invitrogen)
457 in SFM-II medium (Gibco) in a 6-well plate at 28 °C. Virus-containing medium was harvested (P0) after 72
458 hours for infection of $10^6$ cells in Insect-Express medium (Lonza) to be cultured at 28ºC while constant
459 shaking. Cells were harvested by centrifugation after 72 hours and purified using Strep-Tactin Sepharose
460 beads (iba #2-1201-010).
461

462 **NBD-labelling of FAPP1-PH**

463 Labelling of FAPP1-PH was performed according to ref.[37]. In brief, purified protein was incubated with 5-
464 fold excess IANBD-amide overnight (Setareh Biotech #6281) followed by quenching of unbound dye with

465 *L*-cysteine 5-fold excess of the dye. Next, labelled protein was subjected to Zeba Spin desalting column
466 (Thermo Fisher #89890). Labelling efficiency was determined by absorbances at 280nm and 480nm using
467 a NanoDrop.
468

469 **Methyl-β-cyclodextrin and MTT viability assay**

470 Cells were seeded in a 96-well plate and were cultured in OptiMEM (ThermoFisher #31985047) for 3 days.
471 Cells were treated with 10mM methyl-β-cyclodextrin (Sigma #C4555) and cell viability was tested using
472 MTT viability assay (Cayman #21795). Absorbance at 560nm was measured using a BMG ClarioStar plate
473 reader.
474

475 **Liposome preparations**

476 For PS transfer assay using ORDs, donor liposomes composed of 2% NBD-PS (Avanti #810194), 2%
477 Rhodamine-PE (Avanti #810150), 10% DOPE (Avanti #850725), 86% DOPC (Avanti #850375) and
478 acceptor liposomes composed of DOPC with or without 5% brain PI(4)P (Avanti #840045) were used. For
479 PS transfer assays using full-length proteins, donor liposomes composed of 2% NBD-PS, 2% Rhodamine-
480 PE, 2% 18:1 DGS-NTA(Ni) (Avanti# 790404), 10% POPE (Avanti # 850757) and 84% POPC (Avanti
481 #850457) and acceptor liposomes of 85% POPC, 10% POPE and 5% brain PI4P were used. For PI4P
482 transfer assays, donor liposomes were 95% DOPC and 5% POPS (Avanti # 840034) and acceptor
483 liposomes were 93% DOPC and 5% PI4P (Echelon #P-4016), and 2% Rhodamine-PE.
484

485 Lipids were mixed in a glass container and dried under a constant nitrogen flow to create a film. Lipids were
486 freeze-dried at least for two hours under vacuum. Next, lipid films were rehydrated in HKM (50mM HEPES
487 pH 7.2; 120mM potassium acetate; 1mM $MgCl_2$) buffer for 30 minutes followed by 5 cycles of freeze thaw.
488 Lipids were extruded using Avanti MiniExtruder using a 100nm or 200nm filter. Uniformity of lipids were
489 confirmed using a Wyatt Nanostar Dynamic Light Scattering.
490

491 **Lipid transfer assays**

492 For PS transfer assays using ORDs, final concentrations of 80μM of each donor and acceptor vesicles
493 were used in 100μL volume and the indicated amounts of protein of interest was added in 5μL. NBD
494 fluorescence in time was measured using a BMG ClarioStar plate reader. For PS transfer assay using full-
495 length proteins, 100μM of each donor and acceptor vesicles were used with 150nM ORP9, 150nM ORP11
496 and 450nM VAPB-His. Maximum rate of transfer (Vmax) was calculated using a self-starting non-linear
497 least squares function implemented in R (SSmicmen) after background subtraction to no protein control
498 and normalizing to maximum amount of fluorescence obtained after addition of 2% CHAPS. PI4P transfer
499 assay were adapted from ref.[37]. Donor and acceptor liposomes were first incubated with 500nM NBD-
500 labelled FAPP1-PH for 5 minutes before addition of 150nM ORD9 or ORD11. Data was fit using a self-
501 starting non-linear least squares function implemented in R (SSmicmen).
502

503 **Liposome floatation**

504 10μM VAPB-His was incubated 360μM liposomes containing NTA-DGS lipids in 100μL HKM buffer for
505 30min at RT before mixing with 0.3mL HKM buffer containing 54% sucrose to obtain final concentration of

506 40.5% sucrose. Samples were laid at the bottom of an ultracentrifuge tube and cushioned with HKM buffer
507 containing 30% and 0% sucrose. Samples were centrifuged at 200,000x*g* for 2 hours at 4ºC and fractions
508 were collected for Coomassie blue staining.
509
510 **Liposome tethering**
511 100nM of each ORP9, ORP11 and VAPB-His were incubated with donor and acceptor liposomes for 1h at
512 RT. Diameter of liposomes were measured using a Wyatt Nanostar Dynamic Light Scattering.
513
514 **AlphaFold & AlphaFold-multimer predictions**
515 Structure predictions were performed using AlphaFold, AlphaFold-Multimer and ColabFold prediction tools,
516 as described[66–68].
517
518 **Golgi isolation and quantification of Golgi lipid levels**
519 Cells were washed twice with 0.25M Sucrose and scraped in IM buffer (0.25M Mannitol, 0.5mM EGTA,
520 5mM HEPES pH 7.4). Samples were passed through a 26xG needle for lysis. Lysates were cleared from
521 nuclei by centrifugation twice at 600xg for 5min. Post-nuclear supernatant was subjected to protein
522 determination using BCA protein determination kit. Equal amounts of protein were supplemented with
523 150mM NaCl and incubated with Protein A/G Magnetic Beads (ThermoFisher #88802) preloaded either or
524 not with Golgin-97 antibody. Next, samples were washed 3 times with IM buffer supplemented with 150mM
525 NaCl before lipid extraction for lipidomics analysis (described above) or enzymatic activity assay (described
526 below). Amounts of Golgi fractions isolated from different knockouts were confirmed by western blotting.
527
528 **siRNA transfections and metabolic chasing of BODIPY-C5-ceramide in intact cells**
529 siRNA transfections were carried out as described previously[27]. siRNA for UGCG (M-006441-02-0005)
530 and UGT8 (M-010270-02-0005) were obtained from Horizon Discovery. MelJuSo cells treated with siRNAs
531 or 10μM PDMP (Cayman #62595) were washed twice with PBS and incubated with serum-free medium
532 supplemented with 0.25μM BODIPY-C5-Ceramide complexed to BSA (Thermo Fisher #B22650). After 3
533 hours, cells were subjected to lipid extraction and thin layer chromatography as described below. The
534 following lipids were used as standards: TopFlour-C11-galactosylceramide (Avanti Polar Lipids #810266),
535 TopFlour-C11-glucosylceramide (Avanti Polar Lipid #810267) and BODIPY- C5-Lactosylceramide (Thermo
536 Fisher #B34402).
537
538 **Metabolic chasing of de novo sphingomyelin synthesis**
539 Cells were incubated with 20μM ethanolic palmitic acid alkyne (Cayman Chemical #13266) in serum-free
540 medium for 6 hours. Next, cells were washed twice in PBS and scraped in 2%NaCl solution. Lysates were
541 subjected to protein determination using Pierce BCA Protein Kit (Thermo #23225) and equal amounts of
542 proteins were used for lipid extractions as above. For alkaline hydrolysis, dried lipids were resuspended in
543 200μL methanolic sodium methoxide and incubated at room temperature for 1h. Samples were added 30μL
544 acetic acid/water (1:4, v/v), 120μL 2% NaCl, and 400μL chloroform to re-extract lipids. Dried lipids were
545 resuspended in 15μL chloroform and 65μL of click mix containing 400μM 3-Azido-7-hydroxycoumarin

546 (Baseclick #BCFA-047-1) and 900μM tetrakis(acetonitrile)copper(I) tetrafluoroborate (Sigma #677892) in
547 acetonitrile/ethanol (7:3, v/v) was added and incubated 3h at 45ºC prior to TLC analysis.
548

549 **Quantitative RT-PCR**

550 RT-PCR was performed as described previously[27] using the following primer sets:
551 CERT_1: ATGTCGGATAATCAGAGCTGGA / ATCCTGCCACCCATGAATGTA,
552 CERT_2: TCCATCTGTCTTAGCAAGGCT / GCTGTTCAATGGCATCTATCCA,
553 SMS1_1: TGTGCCGAGTCTCCTCTGA / CCGTTCTTGTGTGCTTCCAAA,
554 SMS1_2: CAGCATCAAGATTAAACCCAACG / TGGTGAGAACGAAACAGGAAAG,
555 SMS2_1: TCCTACGAACACTTATGCAAGAC / CCGGGTACTTTTTGGTGCCT,
556 SMS2_2: CAAATTGCTATGCCCACTGAATC / GTTGTCAAGACGAGGTTGAAAAC
557

558 **Enzymatic activity assay in lysates and isolated Golgi fractions**

559 For enzymatic activity measurements in lysates, cells were washed twice in 0.25M Sucrose and scraped in
560 IM buffer (0.25M Mannitol, 0.5mM EGTA, 5mM HEPES pH 7.4). Samples were passed through a 26xG
561 needle for lysis. Lysates were cleared from nuclei by centrifugation twice at 600xg for 5min. Post-nuclear
562 supernatant was subjected to protein determination using BCA protein determination kit. Equal amounts of
563 protein in a 50μL volume were mixed with 50μL IM buffer supplemented with 5μM NBD-C6-ceramide
564 (Avanti Polar Lipids #8102109) from an ethanolic solution. Reactions were incubated 1h at 37ºC in dark
565 with constant shaking. Next, samples were subjected to lipid extractions and thin-layer chromatography as
566 described. For the enzymatic activity assays in Golgi, isolated Golgi fractions were resuspended in 50μL
567 IM buffer and incubated with NBD-C6-ceramide as above.
568

569 **Thin-layer chromatography**

570 Dried lipids were spotted on a thin-layer chromatography (TLC) Silica gel 60 (Merck #1.05554.0001) plate
571 and developed in chloroform:methanol:acetone:acetic acid:water (50:10:20:10:5, v/v/v/v/v). Fluorescent
572 images were acquired using a Typhoon FLA9500 equipped with a 488nm laser and a BPB1 filter
573 (530DF20).
574

575 **Gene expression analysis**

576 Gene expression profiles from 947 cancer cell lines were obtained from the Cancer Cell Line
577 Encyclopedia[69].
578

579 **Plasmids**

| ***Plasmid*** | ***Reference*** | ***cDNA*** | ***Backbone*** |
|---|---|---|---|
| GST-EQT-GFP | This study | IDT GeneBlock | pNKI1.8 |
| Scarlet-ORP9 iso.2 | This study | Mouse Osbpl9 isoform 2 cDNA was ordered from Horizon Discovery. BC023759. IMAGE:5344071 | mScarlet-C1 |
| Scarlet-ORP11 | | Human OSBPL11 cDNA was ordered from Horizon Discovery. IMAGE:3916115. BC065213 | mScarlet-C1 |

| | | | |
|---|---|---|---|
| GFP-OSBP-PH | addgene #49571, ref.[42] | | |
| RFP-LactC2 | addgene#74061, ref.[41] | | |
| mCherry-PKD/C1ab | addgene# 139314, ref.[70] | | |
| GFP-CC11 | This study | | |
| Mito-tagRFP | This study | cDNA encoding the first 70 amino acids of TOM70 was ordered from IDT technologies. | tagRFP-N1 |
| Mito-CC9-tagRFP | This study | | tagRFP-N1 |
| GFP-PH9 | This study | | meGFP-C1 |
| GFP-PH11 | This study | | meGFP-C1 |
| GFP-PH9-PH11 | This study | | meGFP-C1 |
| FLAG-ORP11 | This study | | FLAG-C1 |
| GST-ORD9 | This study | | pNKI1.8 |
| GST-ORD11 | This study | | pNKI1.8 |
| GST-FAPP1-PH | This study | IDT GeneBlock | pNKI1.8 |
| GST-VAPBΔTM-His | This study | Ref.[27] | pNKI1.8 |
| Strep-ORP9 | This study | | |
| Strep-ORP11 | This study | | |
| FLAG-VAPA | Ref.[27] | | |
| meGFP-C1 | Ref.[27] | | |
| mScarlet-C1 | Ref.[27] | | |
| GFP-VAPA | Ref.[27] | | |
| GFP-VAPA** | Ref.[27] | | |
| Scarlet-CERT | Ref.[27] | | |

580

581 **Antibodies**

| Target | Supplier | Catalog # | Host |
|---|---|---|---|
| OSBP | Proteintech | 11096-1-AP | Rabbit |
| ORP1L | PMID: 12631712 | | Rabbit |
| CERT | Bethyl | A300-669A | Rabbit |
| NPC1 | Novus | NB400-148 | Rabbit |
| NPC2 | Proteintech | 19888-1-AP | Rabbit |
| GLTP | Proteintech | 10850-1-AP | Rabbit |
| PITPNB | Proteintech | 13110-1-AP | Rabbit |
| ORP9 | Proteintech | 11879-1-AP | Rabbit |
| STARD7 | Proteintech | 15689-1-AP | Rabbit |
| SEC14L1 | Proteintech | 25541-1-AP | Rabbit |
| PITNM1 | Proteintech | 26983-1-AP | Rabbit |
| SEC14L2 | Origene | TA503723 | Mouse |
| TEX2 | Bethyl | A304-705A | Rabbit |
| FAPP2 | Proteintech | 15410-1-AP | Rabbit |
| ORP9 | Santa Cruz | sc-398961 | Mouse |
| CD63-V450 | BD Horizon | 561984 | Mouse |
| CTB-Alexa568 | Invitrogen | C34777 | |
| Actin | Sigma-Aldrich | A5441 | Mouse |
| GM130 | BD Transduction | 610823 | Mouse |
| FLAG-HRP | Sigma-Aldrich | A8592 | Mouse |

| | | | |
|---|---|---|---|
| GFP | Ref.[27] | | Rabbit |
| Scarlet | ChromoTek | 6G6-100 | Mouse |
| tagRFP | Evrogen | AB232 | Rabbit |
| Golgin-97 | Invitrogen | A-21270 | Mouse |
| Golgin-97 | Cell Signaling | 13192S | Rabbit |
| Calnexin (C5C9) | Cell Signaling | 2679 | Rabbit |
| R-PDI | Cell Signaling | 3501 | Rabbit |
| TOM20 | Proteintech | 11802-1-AP | Rabbit |
| Actin*HRP | Santa Cruz | sc-47778 | Mouse |
| SMS1 | Sigma/Aldrich | HPA045191 | Rabbit |
| SMS2 | Santa Cruz | sc-293384 | Mouse |
| CERT | Proteintech | 15191-1-AP | Rabbit |
| SMS1 | Proteintech | 19050-1-AP | Rabbit |
| ORP11 | Proteintech | 11318-1-AP | Rabbit |
| Anti-mouse Alexa 488 | Thermo Fisher | A21202 | Donkey |
| Anti-mouse Alexa 568 | Thermo Fisher | A10037 | Donkey |
| Anti-mouse Alexa 647 | Thermo Fisher | A21236 | Goat |
| Anti-rabbit Alexa 488 | Thermo Fisher | A21206 | Donkey |
| Anti-rabbit Alexa 568 | Thermo Fisher | A10042 | Donkey |
| Anti-rabbit Alexa 647 | Thermo Fisher | A31573 | Donkey |
| Anti-Mouse IgG, HRP | Thermo Fisher | G21040 | Goat |
| Anti-Rabbit, IgG, HRP | Thermo Fisher | G21234 | Goat |
| Anti-Mouse IgM, Alexa Fluor 488 | Thermo Fisher | A-21042 | Goat |
| Anti-PtdIns(4)P | Echelon | Z-P004 | Mouse IgM |

582

583

584

**References:**


1. van Meer, G. & de Kroon, A. I. P. M. Lipid map of the mammalian cell. *J. Cell Sci.* **124**, 5–8 (2011).
2. Wong, L. H., Gatta, A. T. & Levine, T. P. Lipid transfer proteins: the lipid commute via shuttles, bridges and tubes. *Nature Reviews Molecular Cell Biology* vol. 20 85–101 (2019).
3. Chiapparino, A., Maeda, K., Turei, D., Saez-Rodriguez, J. & Gavin, A. C. The orchestra of lipid-transfer proteins at the crossroads between metabolism and signaling. *Prog. Lipid Res.* **61**, 30–39 (2016).
4. Scorrano, L. *et al.* Coming together to define membrane contact sites. *Nat. Commun.* **10**, 1–11 (2019).
5. Prinz, W. A., Toulmay, A. & Balla, T. The functional universe of membrane contact sites. *Nat. Rev. Mol. Cell Biol.* **21**, (2019).
6. Gatta, A. T. *et al.* A new family of StART domain proteins at membrane contact sites has a role in ER-PM sterol transport. *Elife* **4**, 1–46 (2015).
7. Sandhu, J. *et al.* Aster Proteins Facilitate Nonvesicular Plasma Membrane to ER Cholesterol Transport in Mammalian Cells. *Cell* **175**, 514-529.e20 (2018).
8. Valverde, D. P. *et al.* ATG2 transports lipids to promote autophagosome biogenesis. *J. Cell Biol.* **218**, 1787–1798 (2019).
9. Osawa, T. *et al.* Atg2 mediates direct lipid transfer between membranes for autophagosome formation. *Nat. Struct. Mol. Biol.* **26**, 281–288 (2019).
10. Yeo, H. K. *et al.* Phospholipid transfer function of PTPIP51 at mitochondria-associated ER membranes. *EMBO Rep.* **22**, (2021).
11. Kumar, N. *et al.* VPS13A and VPS13C are lipid transport proteins differentially localized at ER contact sites. *J. Cell Biol.* **217**, 3625–3639 (2018).
12. Castro, I. G. *et al.* Systematic analysis of membrane contact sites in Saccharomyces cerevisiae uncovers modulators of cellular lipid distribution. *Elife* **11**, (2022).
13. Neuman, S. D., Levine, T. P. & Bashirullah, A. A novel superfamily of bridge-like lipid transfer proteins. *Trends Cell Biol.* **32**, 962–974 (2022).
14. Holthuis, J. C. M. & Menon, A. K. Lipid landscapes and pipelines in membrane homeostasis. *Nature* **510**, 48–57 (2014).
15. Hanada, K. *et al.* Molecular machinery for non-vesicular trafficking of ceramide. *Nature* **426**, 803–809 (2003).
16. Wong, C. H. *et al.* Genome-scale requirements for dynein-based trafficking revealed by a high-content arrayed CRISPR screen. *bioRxiv* 2023.03.01.530592 (2023) doi:10.1101/2023.03.01.530592.
17. Reza, S., Ugorski, M. & Suchański, J. Glucosylceramide and galactosylceramide, small glycosphingolipids with significant impact on health and disease. *Glycobiology* vol. 31 1416–1434 (2021).
18. Nurmi, H. *et al.* Glycolipid transfer protein knockout disrupts vesicle trafficking to the plasma membrane. *J. Biol. Chem.* **299**, 104607 (2023).
19. Platt, F. M. Sphingolipid lysosomal storage disorders. *Nature* **510**, 68–75 (2014).
20. Newton, J., Milstien, S. & Spiegel, S. Niemann-Pick type C disease: The atypical sphingolipidosis. *Adv. Biol. Regul.* **70**, 82–88 (2018).
21. Sokoya, T. *et al.* Pathogenic variants of sphingomyelin synthase SMS2 disrupt lipid landscapes in the secretory pathway. *Elife* **11**, (2022).
22. Deng, Y., Rivera-Molina, F. E., Toomre, D. K. & Burd, C. G. Sphingomyelin is sorted at the trans Golgi network into a distinct class of secretory vesicle. *Proc. Natl. Acad. Sci. U. S. A.* **113**, 6677–6682 (2016).
23. Kumagai, K. & Hanada, K. Structure, functions and regulation of CERT, a lipid-transfer protein for the delivery of ceramide at the ER–Golgi membrane contact sites. *FEBS Lett.* **593**, 2366–2377 (2019).
24. Zhou, Y. *et al.* OSBP-related protein 11 (ORP11) dimerizes with ORP9 and localizes at the Golgi-late endosome interface. *Exp. Cell Res.* **316**, 3304–3316 (2010).
25. Neefjes, J. & Cabukusta, B. What the VAP: The Expanded VAP Family of Proteins Interacting With FFAT and FFAT-Related Motifs for Interorganellar Contact. *Contact* **4**, 251525642110122 (2021).
26. Di Mattia, T. *et al.* Identification of MOSPD2, a novel scaffold for endoplasmic reticulum membrane contact sites. *EMBO Rep.* **19**, 1–22 (2018).
27. Cabukusta, B. *et al.* Human VAPome Analysis Reveals MOSPD1 and MOSPD3 as Membrane Contact Site Proteins Interacting with FFAT-Related FFNT Motifs. *Cell Rep.* **33**, 108475 (2020).
28. Levine, T. P. & Munro, S. The pleckstrin homology domain of oxysterol-binding protein recognises a determinant specific to Golgi membranes. *Curr. Biol.* **8**, 729–739 (1998).
29. Levine, T. P. & Munro, S. Targeting of Golgi-specific pleckstrin homology domains involves both PtdIns 4-kinase-dependent and -independent components. *Curr. Biol.* **12**, 695–704 (2002).
30. Wang, H. *et al.* ORP2 Delivers Cholesterol to the Plasma Membrane in Exchange for

Phosphatidylinositol 4, 5-Bisphosphate (PI(4,5)P 2 ). *Mol. Cell* **73**, 458-473.e7 (2019).
31. Mesmin, B. *et al.* A four-step cycle driven by PI(4)P hydrolysis directs sterol/PI(4)P exchange by the ER-Golgi Tether OSBP. *Cell* **155**, 830–843 (2013).
32. de Saint-Jean, M. *et al.* Osh4p exchanges sterols for phosphatidylinositol 4-phosphate between lipid bilayers. *J. Cell Biol.* **195**, 965–978 (2011).
33. Maeda, K. *et al.* Interactome map uncovers phosphatidylserine transport by oxysterol-binding proteins. *Nature* **501**, 257–261 (2013).
34. Tan, J. X. & Finkel, T. A phosphoinositide signalling pathway mediates rapid lysosomal repair. *Nature* **609**, 815–821 (2022).
35. Kawasaki, A. *et al.* PI4P/PS countertransport by ORP10 at ER–endosome membrane contact sites regulates endosome fission. *J. Cell Biol.* **221**, (2021).
36. He, R. *et al.* ORP9 and ORP10 form a heterocomplex to transfer phosphatidylinositol 4-phosphate at ER-TGN contact sites. *Cell. Mol. Life Sci.* **80**, 77 (2023).
37. Ikhlef, S. *et al.* Functional analyses of phosphatidylserine/PI(4)P exchangers with diverse lipid species and membrane contexts reveal unanticipated rules on lipid transfer. *BMC Biol.* **19**, 248 (2021).
38. Chung, J. *et al.* PI4P/phosphatidylserine countertransport at ORP5- and ORP8-mediated ER - Plasma membrane contacts. *Science (80-. ).* **349**, 428–432 (2015).
39. Von Filseck, J. M. *et al.* Phosphatidylserine transport by ORP/Osh proteins is driven by phosphatidylinositol 4-phosphate. *Science (80-. ).* **349**, 432–436 (2015).
40. Posor, Y., Jang, W. & Haucke, V. Phosphoinositides as membrane organizers. *Nat. Rev. Mol. Cell Biol.* **23**, 797–816 (2022).
41. Yeung, T. *et al.* Membrane phosphatidylserine regulates surface charge and protein localization. *Science* **319**, 210–213 (2008).
42. Moorhead, A. M., Jung, J. Y., Smirnov, A., Kaufer, S. & Scidmore, M. A. Multiple host proteins that function in phosphatidylinositol-4-phosphate metabolism are recruited to the chlamydial inclusion. *Infect. Immun.* **78**, 1990–2007 (2010).
43. Kol, M. *et al.* Switching head group selectivity in mammalian sphingolipid biosynthesis by active-site-engineering of sphingomyelin synthases. *J. Lipid Res.* **58**, 962–973 (2017).
44. Tafesse, F. G., Ternes, P. & Holthuis, J. C. M. The multigenic sphingomyelin synthase family. *J. Biol. Chem.* **281**, 29421–29425 (2006).
45. Capasso, S. *et al.* Sphingolipid metabolic flow controls phosphoinositide turnover at the trans-Golgi network. *EMBO J.* **36**, 1736–1754 (2017).
46. Peretti, D., Dahan, N., Shimoni, E., Hirschberg, K. & Lev, S. Coordinated lipid transfer between the endoplasmic reticulum and the Golgi complex requires the VAP proteins and is essential for Golgi-mediated transport. *Mol. Biol. Cell* **19**, 3871–3884 (2008).
47. Horibata, Y. & Sugimoto, H. StarD7 mediates the intracellular trafficking of phosphatidylcholine to mitochondria. *J. Biol. Chem.* **285**, 7358–7365 (2010).
48. Saita, S. *et al.* PARL partitions the lipid transfer protein STARD7 between the cytosol and mitochondria. *EMBO J.* **37**, 1–18 (2018).
49. Horibata, Y. *et al.* StarD7 protein deficiency adversely affects the phosphatidylcholine composition, respiratory activity, and cristae structure of mitochondria. *J. Biol. Chem.* **291**, 24880–24891 (2016).
50. Venditti, R. *et al.* Molecular determinants of ER-Golgi contacts identified through a new FRET-FLIM system. *J. Cell Biol.* **218**, 1055–1065 (2019).
51. Ridgway, N. D., Dawson, P. A., Ho, Y. K., Brown, M. S. & Goldstein, J. L. Translocation of oxysterol binding protein to Golgi apparatus triggered by ligand binding. *J. Cell Biol.* **116**, 307–319 (1992).
52. de la Mora, E. *et al.* Nanoscale architecture of a VAP-A-OSBP tethering complex at membrane contact sites. *Nat. Commun.* **12**, 3459 (2021).
53. Gehin, C. *et al.* CERT1 mutations perturb human development by disrupting sphingolipid homeostasis. *J. Clin. Invest.* **133**, (2023).
54. Peretti, D., Kim, S., Tufi, R. & Lev, S. Lipid Transfer Proteins and Membrane Contact Sites in Human Cancer. *Front. Cell Dev. Biol.* **7**, 1–14 (2020).
55. Mizuike, A. & Hanada, K. DGARM/C10orf76/ARMH3 for Ceramide Transfer Zone at the Endoplasmic Reticulum–Distal Golgi Contacts. *Contact* **7**, 25152564241239444 (2024).
56. Cockcroft, S. & Lev, S. Mammalian PITPs at the Golgi and ER-Golgi Membrane Contact Sites. *Contact* **3**, 2515256420964170 (2020).
57. Radulovic, M. *et al.* Cholesterol transfer via endoplasmic reticulum contacts mediates lysosome damage repair. *EMBO J.* **41**, (2022).
58. Vacaru, A. M. *et al.* Sphingomyelin synthase-related protein SMSr controls ceramide homeostasis in the ER. *J. Cell Biol.* **185**, 1013–1027 (2009).
59. Mesmin, B. *et al.* Sterol transfer, PI 4P consumption, and control of membrane lipid order by endogenous OSBP . *EMBO J.* **36**, 3156–3174 (2017).
60. Doench, J. G. *et al.* Optimized sgRNA design to maximize activity and minimize off-target effects of

711 CRISPR-Cas9. *Nat. Biotechnol.* **34**, 184–191 (2016).
712 61. Sanjana, N. E., Shalem, O. & Zhang, F. Improved vectors and genome-wide libraries for CRISPR
713 screening. *Nat. Methods* **11**, 783–784 (2014).
714 62. Wijdeven, R. H. *et al.* CRISPR Activation Screening Identifies VGLL3-TEAD1-RUNX1/3 as a
715 Transcriptional Complex for PD-L1 Expression. *J. Immunol.* (2022)
716 doi:10.4049/JIMMUNOL.2100917.
717 63. Ghorasaini, M. *et al.* Cross-Laboratory Standardization of Preclinical Lipidomics Using Differential
718 Mobility Spectrometry and Multiple Reaction Monitoring. *Anal. Chem.* **93**, 16369–16378 (2021).
719 64. Su, B. *et al.* A DMS Shotgun Lipidomics Workflow Application to Facilitate High-Throughput,
720 Comprehensive Lipidomics. *J. Am. Soc. Mass Spectrom.* **32**, 2655–2663 (2021).
721 65. Faas, F. G. A. *et al.* Virtual nanoscopy: generation of ultra-large high resolution electron microscopy
722 maps. *J. Cell Biol.* **198**, 457–469 (2012).
723 66. Jumper, J. *et al.* Highly accurate protein structure prediction with AlphaFold. *Nature* **596**, 583–589
724 (2021).
725 67. Mirdita, M. *et al.* ColabFold: making protein folding accessible to all. *Nat. Methods* **19**, 679–682
726 (2022).
727 68. Evans, R. *et al.* Protein complex prediction with AlphaFold-Multimer. *bioRxiv* 2021.10.04.463034
728 (2022) doi:10.1101/2021.10.04.463034.
729 69. Barretina, J. *et al.* The Cancer Cell Line Encyclopedia enables predictive modelling of anticancer
730 drug sensitivity. *Nature* **483**, 603–607 (2012).
731 70. Zewe, J. P., Wills, R. C., Sangappa, S., Goulden, B. D. & Hammond, G. R. SAC1 degrades its lipid
732 substrate PtdIns4P in the endoplasmic reticulum to maintain a steep chemical gradient with donor
733 membranes. *Elife* **7**, (2018).
734

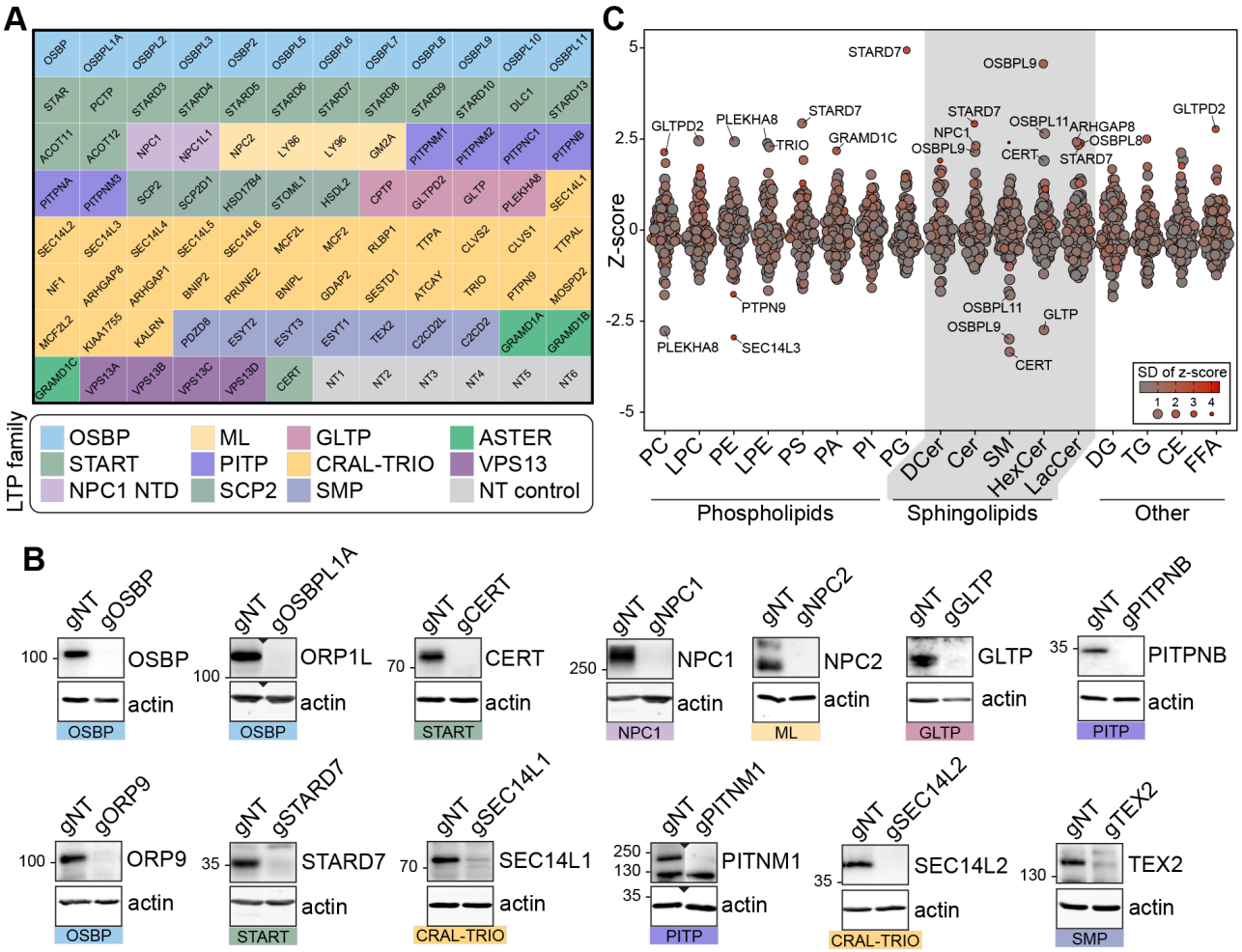


**Figure 1: Lipidomics analysis of a LTP knockout library revealed known and candidate controllers of cellular lipid levels.**

(A) Overview of the arrayed gene knockout library targeting LTPs. NT: non-targeting. (B) Western blotting of the selected wells showing the efficiency of the LTP knockout library on MelJuSo cells. gNT: Non-targeting, control cells. (C) Summary plot of the lipidomics analysis: Z-scores calculated for 17 lipid classes are plotted. Each data point represents the mean Z-score of an LTP knockout cell line; size and color of data points represent the standard deviation of Z-scores for 3 experiments on average. PC: phosphatidylcholine, LPC: lyso-phosphatidylcholine, PE: phosphatidylethanolamine, LPE: lyso-phosphatidylethanolamine, PS: phosphatidylserine, PI: phosphatidylinositol, PA: phosphatidic acid, PG: phosphatidylglycerol, DCer: dihydroxyceramide, Cer: ceramide, SM: sphingomyelin, HexCer: hexosylceramide, LacCer: lactosylceramide, DG: diacylglycerol, TG: triacylglycerol, CE: cholesterol ester, FFA: free fatty acids.

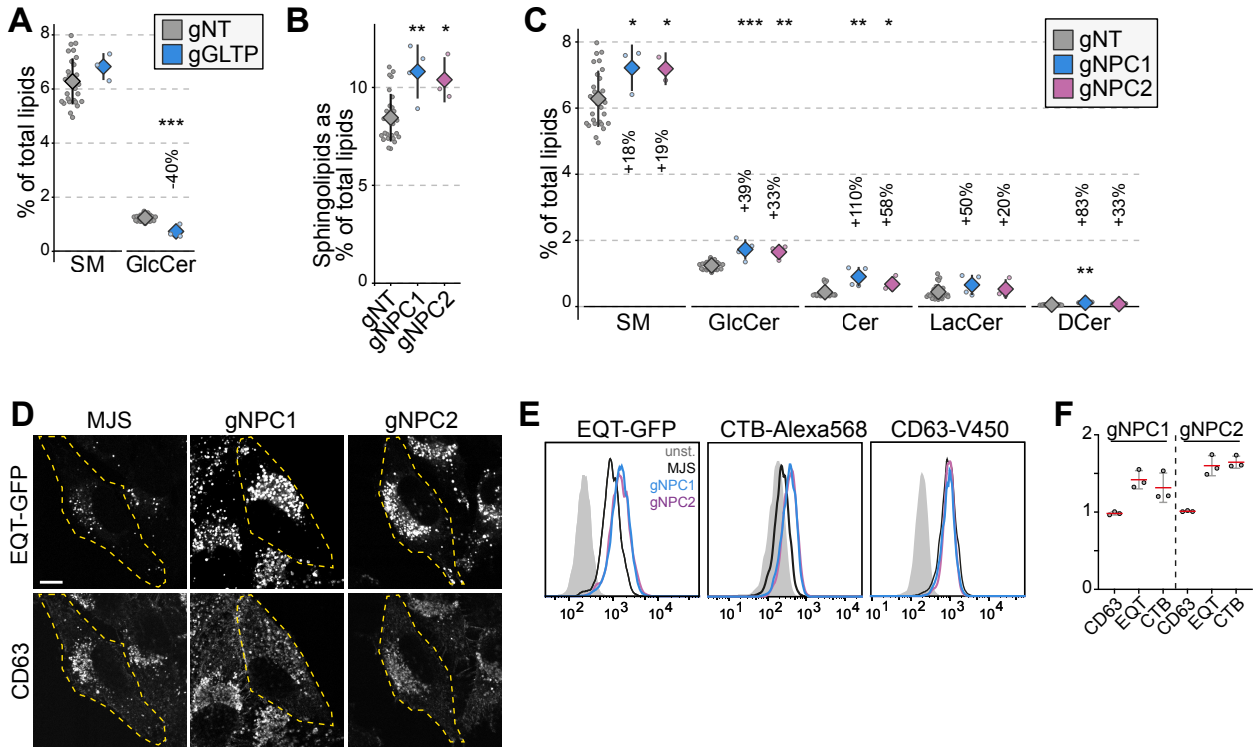


**Figure 2: NPC1 and NPC2 knockout cells accumulate sphingomyelin in lysosomes.**
(A) GLTP knockouts show decreased glucosylceramide levels compared to control cells. GlcCer: glucosylceramide (B) NPC1 and NPC2 knockout cells have increased sphingolipids levels compared to control cells. (C) Increased sphingolipid levels in NPC1 and NPC2 knockouts are represented in all sphingolipid classes. (D) Immunofluorescence images of NPC1 and NPC2 knockout cells permeabilized and stained with recombinant GFP-EQT show the accumulation of sphingomyelin in the lysosomes compared to the parental MelJuSo (MJS) cells. Pixel intensities of the images were adjusted evenly. Scale bar 10µm. (E) Flow cytometry analysis of cells stained with EQT-GFP, CTB-Alexa568 and CD63-V450 on the cell surface. Analysis demonstrates the accumulation of sphingomyelin (EQT-GFP) and the glycosphingolipid GM1 (CTB-Alexa568) on the cell surface without affecting the surface protein levels. (F) Mean fluorescence intensities for each staining normalized to control cells from 3 experiments. Red lines and error bars correspond to mean and standard deviations from 3 experiments, respectively. Approximately 2000 cells were analyzed per experiment.

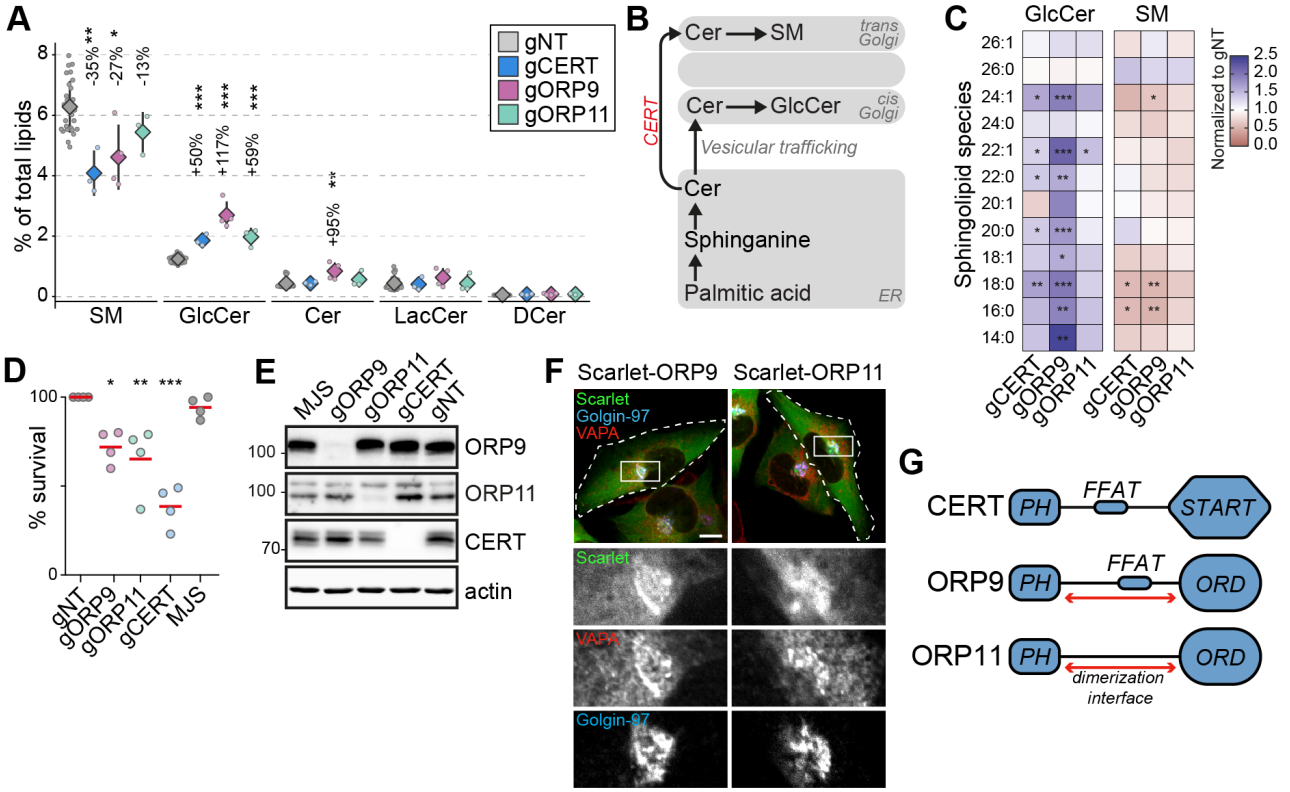


**Figure 3: CERT, ORP9 and ORP11 knockout cells demonstrate reduced sphingomyelin levels.** (A) CERT, ORP9 and ORP11 knockouts demonstrate decreased sphingomyelin and increased glucosylceramide levels. (B) Schematic representation of *de novo* sphingomyelin synthesis pathway of mammalian cells. (C) Decreased sphingomyelin and increased glucosylceramide levels observed in knockout cells are present in various sphingolipid subspecies. (D) Similar to CERT knockouts, ORP9 and ORP11 knockouts are sensitive to methyl-β-cyclodextrin treatment. Red lines correspond to mean values from 4 experiments. (E) Western blot of knockout cells showing that the loss of ORP9 or ORP11 does not affect CERT protein levels. (F) ORP9 and ORP11 localize at the Golgi apparatus. Scale bar 10µm. (G) Domain architecture of CERT, ORP9 and ORP11. All proteins contain PH domains for Golgi localization. CERT and ORP9, but not ORP11, contain a FFAT motif for interacting with VAP proteins.

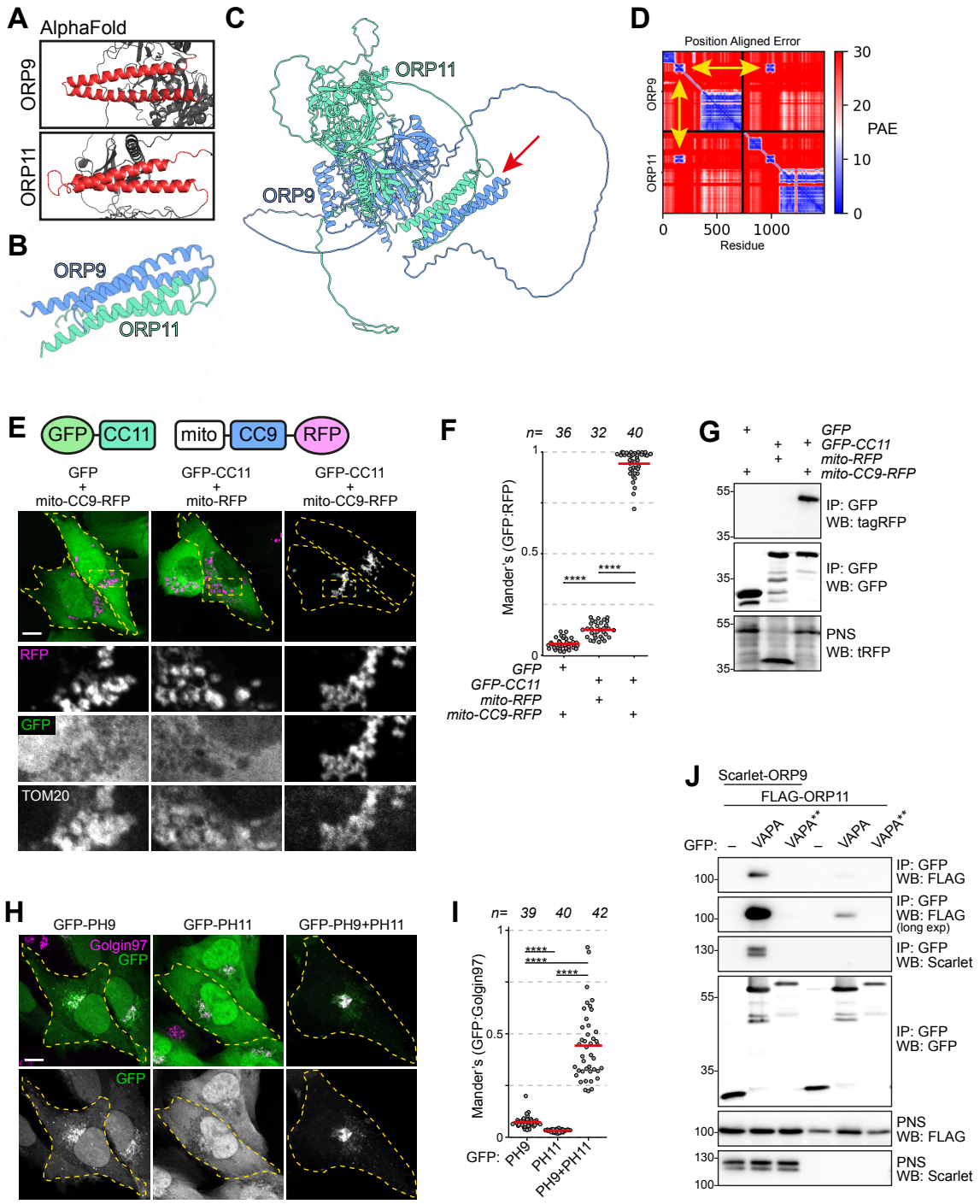


**Figure 4: ORP9 dimerization is critical for ER localization of ORP11.**
(A) AlphaFold revealing coiled coils in ORP9 and ORP11. (B) AlphaFold-Multimer shows that coiled coils of ORP9 and ORP11 interacting with each other. (C) ColabFold protein complex prediction for full length ORP9 and ORP11 shows the dimerization via coiled coils (arrow). (D) Position aligned error for panel C. Note that the interaction of coils has a lower score (yellow arrows). (E) Coiled coils of ORP9 and ORP11 is sufficient to define their localization as ORP11 coiled coils colocalizes with the mitochondria-targeted ORP9 coiled coils at mitochondria. Scale bar: 10µm. (F) Colocalization analysis of immunofluorescent images corresponding to panel E. Red lines correspond to mean values from 3 experiments; n is number of analyzed cells. (G) Co-immunoprecipitation confirming that the coils of ORP9 and ORP11 interact with each other. (H) Immunofluorescence images of PH domain localizations. Compared to individual PH domains of ORP9 and ORP11, ORP9-ORP11 chimera demonstrates better affinity towards the Golgi. Scale bar: 10µm. (I) Colocalization analysis of immunofluorescent images corresponding to panel H. Red lines correspond to mean values from 3 experiments; n is number of analyzed cells. (J) Co-immunoprecipitation analysis of VAPA, ORP9

and ORP11 from over-expressing cells. Despite lacking a FFAT motif, ORP11 interacts with the ER-resident VAPA protein. This interaction is facilitated by the FFAT motif of ORP9 as a VAPA mutant unable to interact with FFAT motifs (VAPA**) was unable to co-precipitate ORP9 or ORP11.

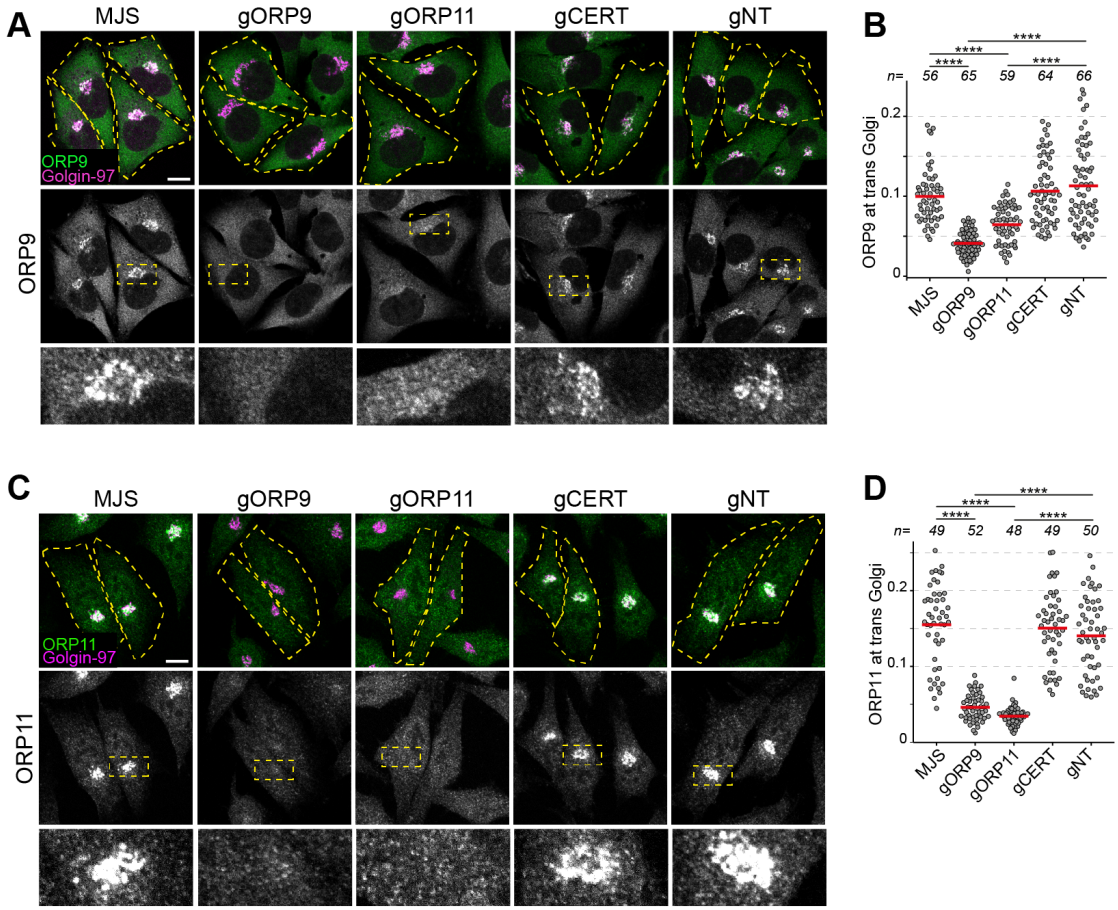


**Figure 5: ORP9 and ORP11 dimerization is critical for their Golgi localization.**
(A) Immunofluorescence images of cells stained for ORP9. ORP9 fails to localize at the Golgi as efficiently in ORP11 knockout cells. (B) Colocalization analysis of immunofluorescent images corresponding to panel A. Red lines correspond to mean values from 3 experiments; n is number of analyzed cells. (C) Immunofluorescence images of cells stained using an ORP11 antibody. Similar to ORP9, ORP11 fails to localize at the Golgi as efficiently in ORP9 knockout cells. Note that the effect of ORP9 loss on ORP11 localization is more dramatic than vice versa. (D) Colocalization analysis of immunofluorescent images from panel C. Red lines correspond to mean values from 3 experiments; n is number of analyzed cells. All scale bars are 10µm.

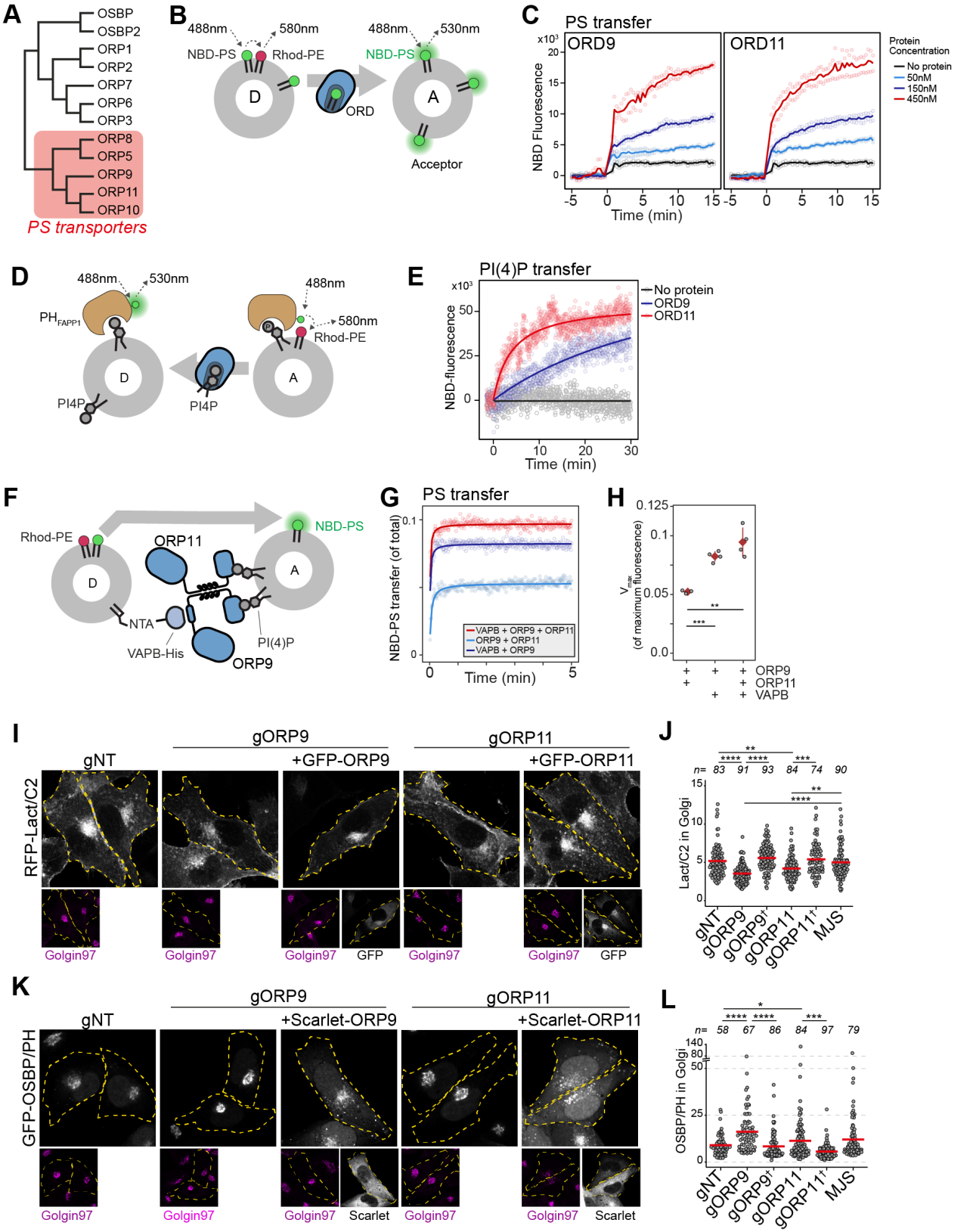


**Figure 6: ORP9 and ORP11 are essential for PS and PI(4)P levels in the Golgi apparatus.**
(A) Phylogenetic tree of human OSBP-related domains showing that ORP9 and ORP11 belong to the PS transporter branch. (B) Schematic representation of FRET-based PS transfer assay. Rhodamine in the donor vesicles quenches NBD fluorescence unless NBD-labeled lipid is transferred to acceptor liposomes. (C) FRET-based lipid transfer assay using the OSBP-related domains of ORP9 and ORP11, ORD9 and ORD11 respectively, demonstrate the PS trafficking ability between vesicles *in vitro*. (D) Graphical representation of PI(4)P transfer assay that utilizes the NBD-labelled PH domain of FAPP1. PI(4)P transfer by a protein leads

to inrease NBD-fluorescence by dequenching. (E) PI(4)P transfer assay using ORP9-ORD and ORP11-ORD (ORD9 and ORD11, respectively). (F) Schematic representation of *in vitro* reconstitution of membrane contact sites for lipid transfer assays. (G) PS transfer assay at *in vitro* reconstituted membrane contact sites formed by the VAPB-ORP9-ORP11 trimer. (H) Vmax quantifications of PS transfer assays from panel E. (I) The PS sensor Lact-C2 localizes less prominently to the Golgi in ORP9 and ORP11 knockout cells. (J) Golgi quantification of the PS sensor RFP-LactC2 indicates reduced PS levels in this organelle. This phenotype could be rescued by reconstitution of the missing protein in knockout cells (shown with a dagger). Red lines correspond to mean values from 3 experiments; n is number of analyzed cells. (K) The PI(4)P sensor OSBP-PH localizes more prominently to the Golgi area in ORP9 and ORP11 knockout cells. (I) Golgi quantification of the PI(4)P sensor confirms the accumulation of PI(4)P at this organelle. This phenotype was rescued by reconstitution of the missing protein in knockout cells (shown with a dagger). Red lines correspond to mean values from 3 experiments; n is number of analyzed cells.

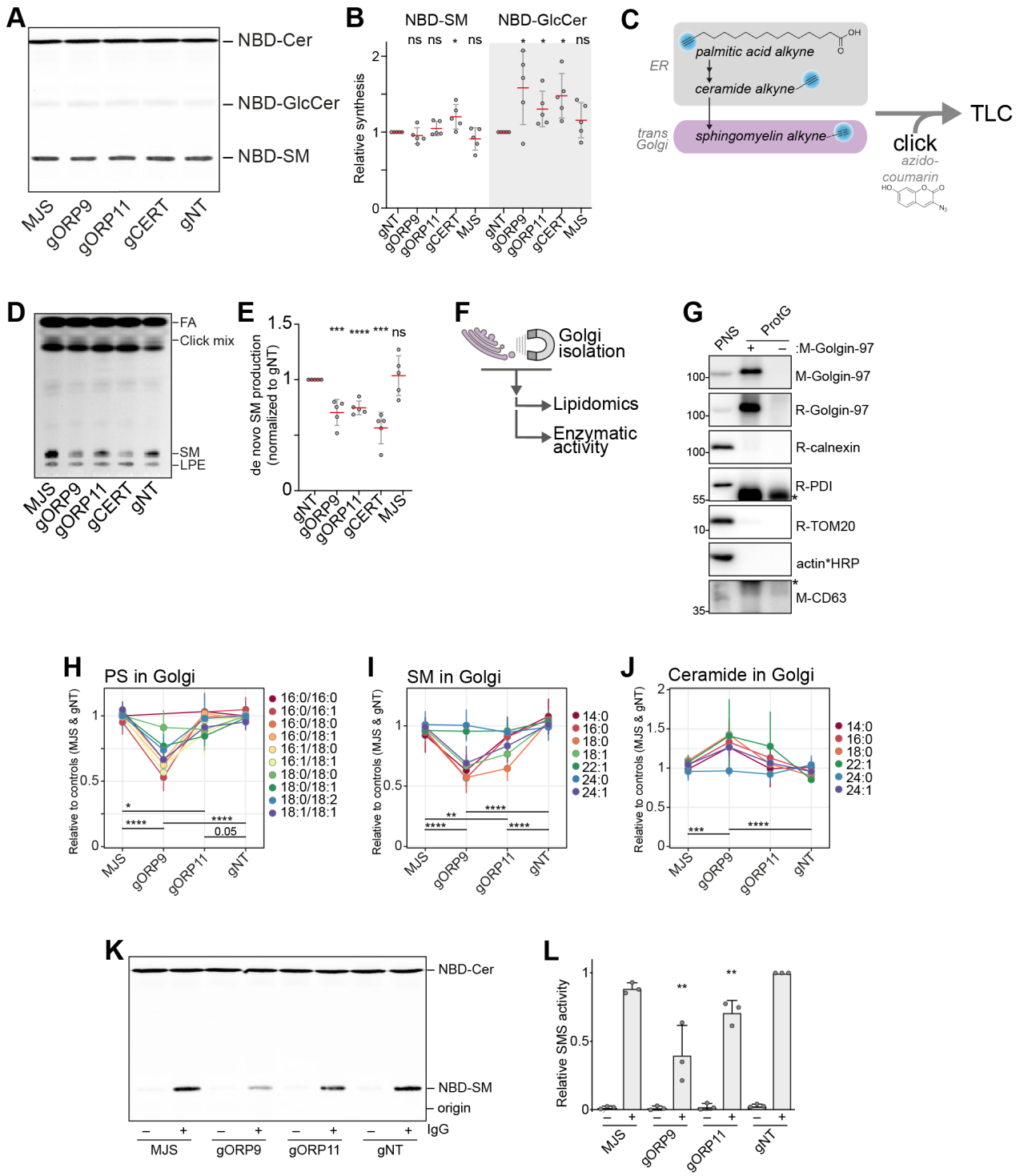


**Figure 7: ORP9 and ORP11 are needed for *de novo* sphingomyelin synthesis in the Golgi apparatus.** (A) Thin-layer chromatography readout of the enzymatic activity assay performed in lysates reveals the unreduced sphingomyelin synthesis capacity of knockout cells. (B) Quantification of the enzymatic activity assays corresponding to panel A. Note the increased GlcCer production capacity in the knockout cells. Red lines and error bars correspond to mean and standard deviation from 5 experiments, respectively. (C) Graphic representation of experiments using palmitic acid alkyne for monitoring *de novo* sphingomyelin synthesis. Alkyne modified sphingolipids are "clicked" with azido-coumarin before thin-layer chromatography (TLC) analysis. (D) TLC readout of *de novo* sphingomyelin synthesis assay in intact cells using palmitic acid alkyne. Knockout cells demonstrate reduced conversion of palmitic acid to sphingomyelin. FA: fatty acid, SM: sphingomyelin, LPE: lyso-O-phosphatidylethanolamine (E) Quantification of *de novo* sphingomyelin synthesis assay from panel C. Red lines and error bars correspond to mean and standard deviation from 5 experiments, respectively. (F) Simplified representation of Golgi-targeted lipidomics and enzymatic activity assays. (G) Western blot confirming the immunomagnetic isolation of *trans* Golgi membranes. Cross-reactivity to Protein

G and/or Golgin-97 IgG were labeled with asterisks. (H-J) Lipidomics analysis of Golgi isolates show lowered PS levels in the Golgi of ORP9 and ORP11 knockout cells. Same Golgi fractions have reduced sphingomyelin but increased ceramide levels. Each colored line corresponds to a lipid species. Data points and the error bars correspond to mean and standard deviations from 4 experiments. (K) TLC readout of enzymatic activity assay performed in isolated Golgi from knockout cells. Golgi of ORP11 and especially that of ORP9 demonstrate lowered capacity to synthesize sphingomyelin. (L) Quantification of sphingomyelin synthesis activity assay performed in Golgi isolates corresponding to panel I.

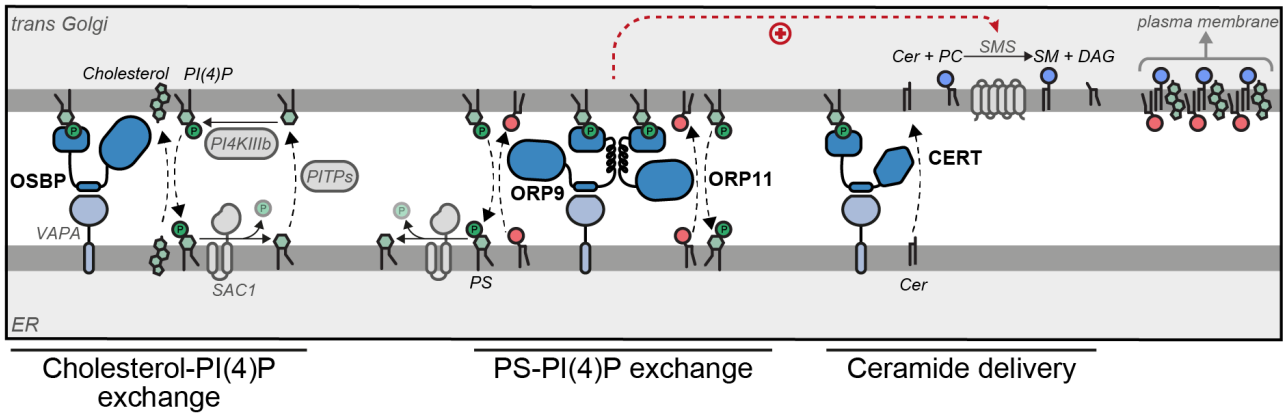


**Figure 8: Model of ORP9-ORP11 mediated promotion of sphingomyelin synthesis at the ER-trans Golgi contact site.**

ORP9 and ORP11 require dimerization with each other to localize at ER-*trans* Golgi membrane contact sites, where they exchange PS for PI(4)P. Consequently loss of either protein causes PS and PI(4)P imbalances in the Golgi apparatus. Since only ORP9 contains a FFAT motif, its loss leads to a more pronounced effect on PS, PI(4)P and sphingolipid levels. The same contact site accommodates other LTPs. Multiple phosphatidylinositol transfer proteins (PITPs) traffic phosphatidylinositol to the Golgi for their phosphorylation. Each PITP at the ER-Golgi contact site serves a different function—one of these proteins, Nir2, also contains a FFAT motif (ref.46 and 54). OSBP and CERT are responsible for the anterograde trafficking of cholesterol and ceramide, the latter is used for sphingomyelin production. Cholesterol, sphingomyelin and PS are trafficked to the plasma membrane by vesicular means to be asymmetrically distributed between the leaflets of the plasma membrane.

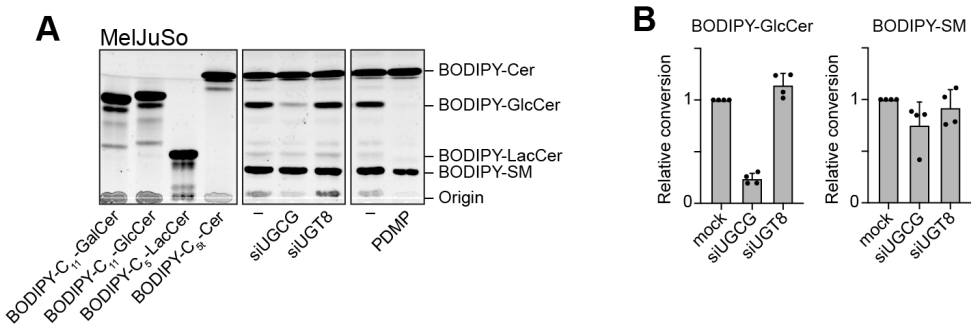


**Supplementary Figure 1: Glucosylceramide is the main hexosylceramide in MelJuSo cells.**
(A) MelJuSo cells silenced for glucosylceramide synthase (siUGCG) or galactosylceramide synthase (siUGT8) or treated with the glucosylceramide synthase inhibitor (PDMP) were fed with the fluorescent ceramide analog BODIPY-C5-ceramide. Lipids were isolated and separated by thin-layer chromatography. Note that the fluorescent band corresponding to monohexosylceramide is affected only when glucosylceramide synthesis is perturbed. (B) Quantifications corresponding to panel A. Bars and error bars correspond to mean and standard deviations from 4 experiments, respectively.

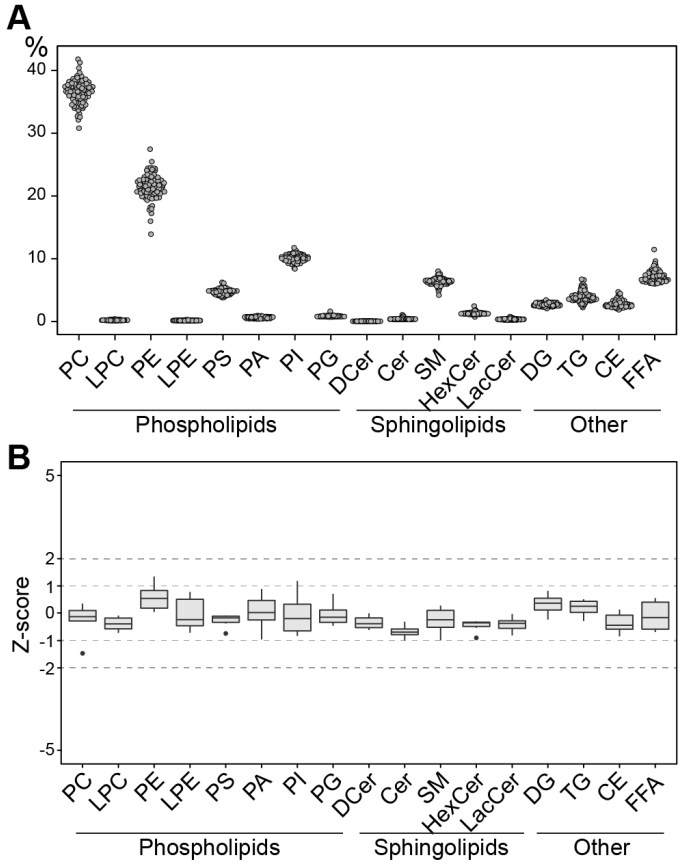


**Supplementary Figure 2: Overview of lipidomics analysis performed for LTP knockout library.**
(A) Percentage distribution of 17 lipid classes in LTP knockout cells; each data point represents the mean percentage of an LTP knockout cell line. (B) Box plots of Z-scores of NT control cells. Note that Z-scores for NT control cells do not exceed the absolute value of 2. PC: phosphatidylcholine, LPC: lysophosphatidylcholine, PE: phosphatidylethanolamine, LPE: lysophosphatidylethanolamine, PS: phosphatidylserine, PA: phosphatidic acid, PG: phosphatidylglycerol, PI: phosphatidylinositol, DCer: dihydroceramide, Cer: ceramide, SM: sphingomyelin, HexCer: hexosyl-ceramide, LacCer: lactosylceramide, DG: diacylglycerol, TG: triacylglycerol, CE: cholesterol ester, and FFA: free fatty acid.

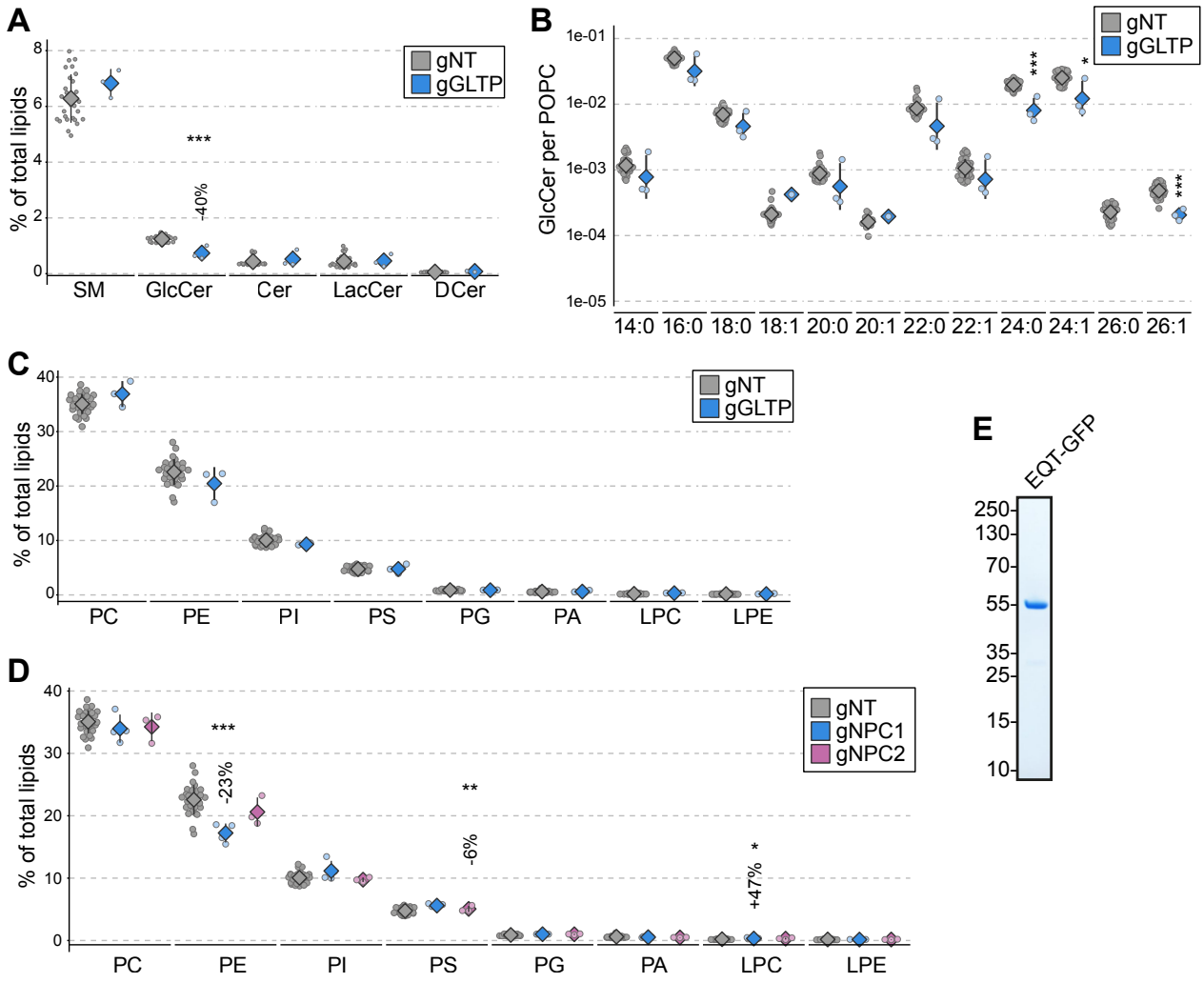


**Supplementary Figure 3: GLTP, NPC1 and NPC2 knockout cells do not display major phospholipid imbalances.**

(A, B) Lipidomics analysis of GLTP knockouts show lowered glucosylceramide levels that is represented in various acyl chain species. (C) GLTP knockouts do not present altered phospholipid levels. (D) Lipidomics analysis of NPC1 and NPC2 knockout cells do not display major changes in their phospholipid repertoire. (E) Coomassie Blue staining of recombinant EQT-GFP.

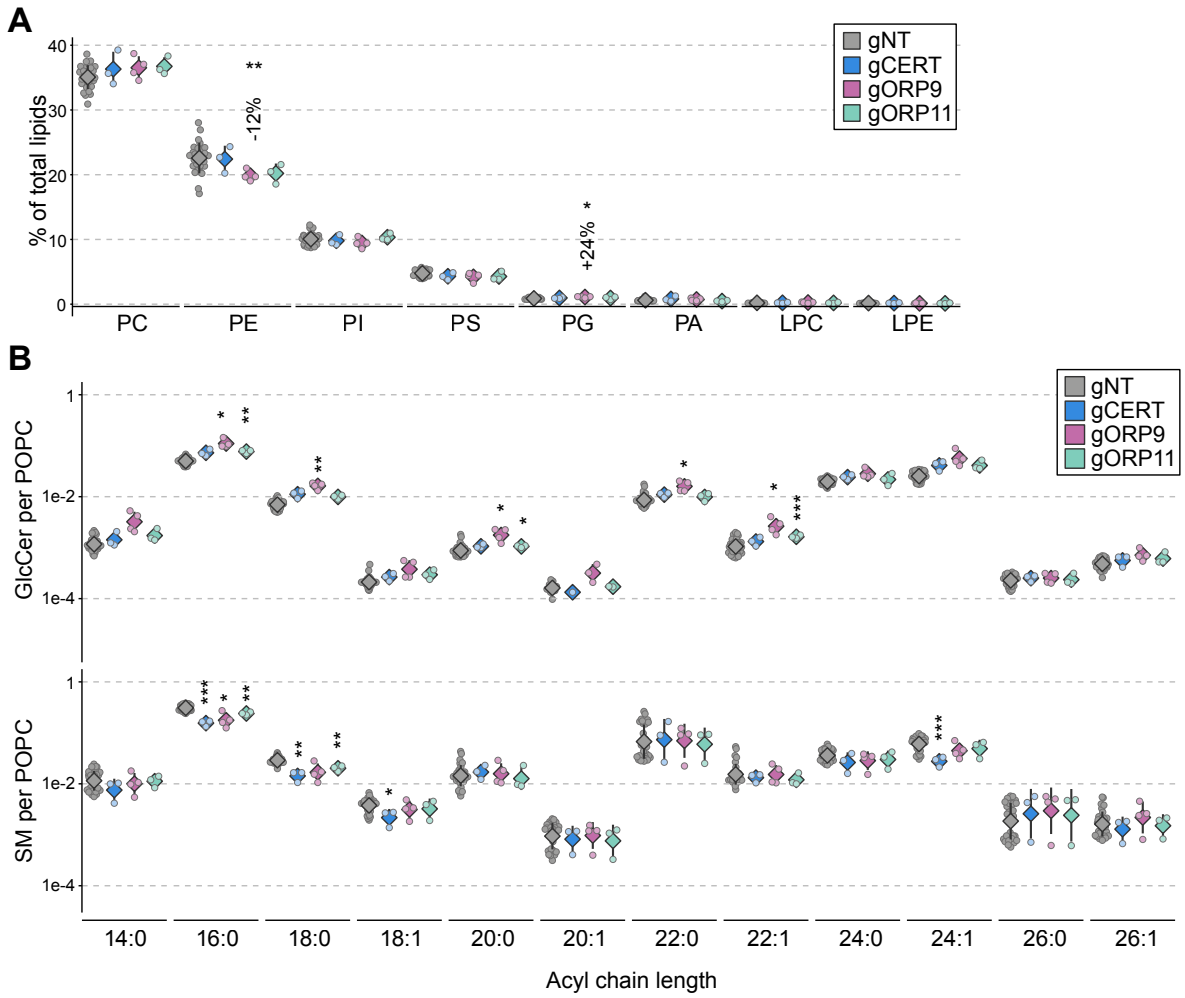


**Supplementary Figure 4: Sphingolipid imbalances in CERT, ORP9 and ORP11 knockouts are represented in multiple acyl chain species.**
(A) CERT, ORP9 and ORP11 knockouts do not display major phospholipid imbalances. (B) Reduced sphingomyelin and increased glucosylceramide levels in CERT, ORP9 and ORP11 knockout cells is observed in multiple acyl chain species. Lipid levels are normalized to the POPC (16:0/18:1) levels.

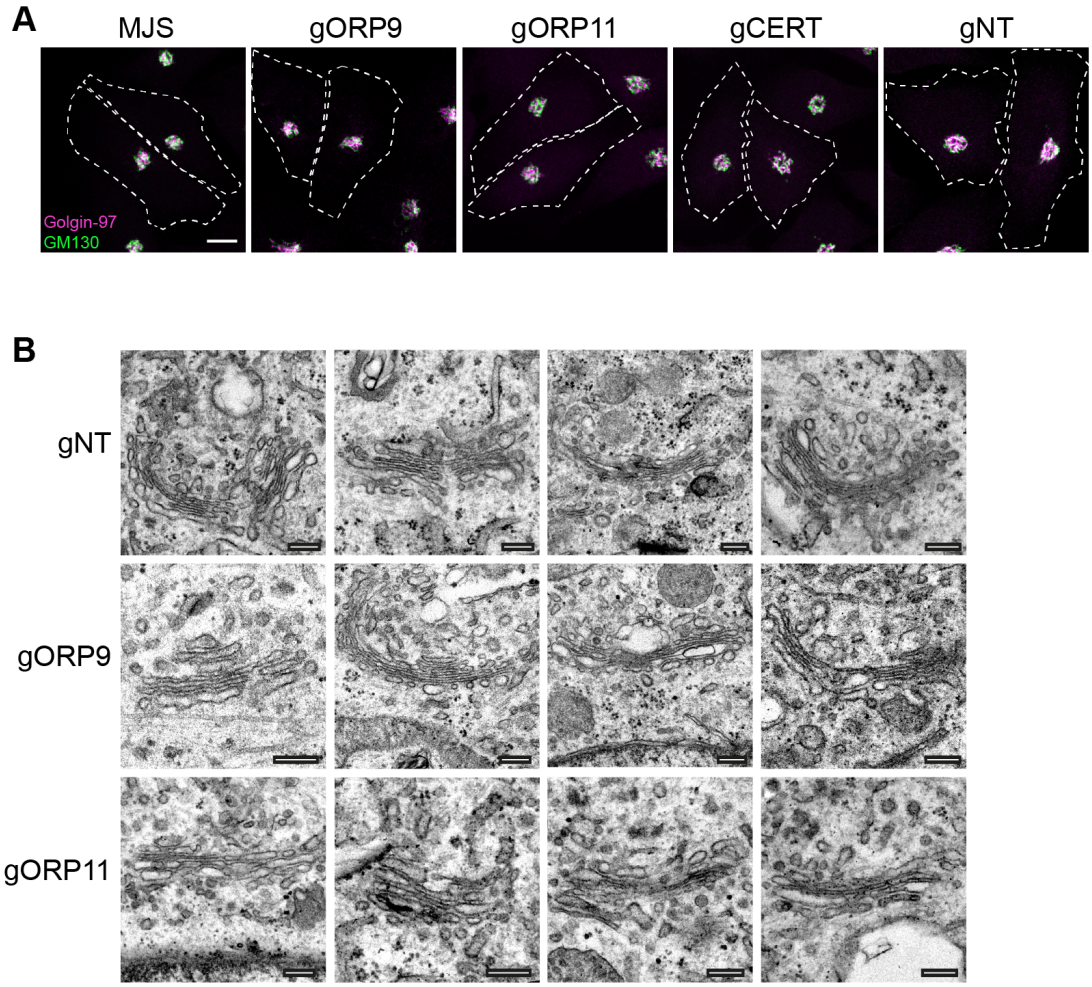


**Supplementary Figure 5: CERT, ORP9 and ORP11 knockouts do not display defects in Golgi morphology.**
(A) Immunofluorescence staining for *cis* and *trans* Golgi markers, GM130 and Golgin-97 respectively, do not show any changes in ORP9, ORP11 and CERT knockouts. Scale bar 10µm. (B) Electron microscopy images for ORP9 and ORP11 knockouts do not display any changes in Golgi morphology. Scale bar 250nm.

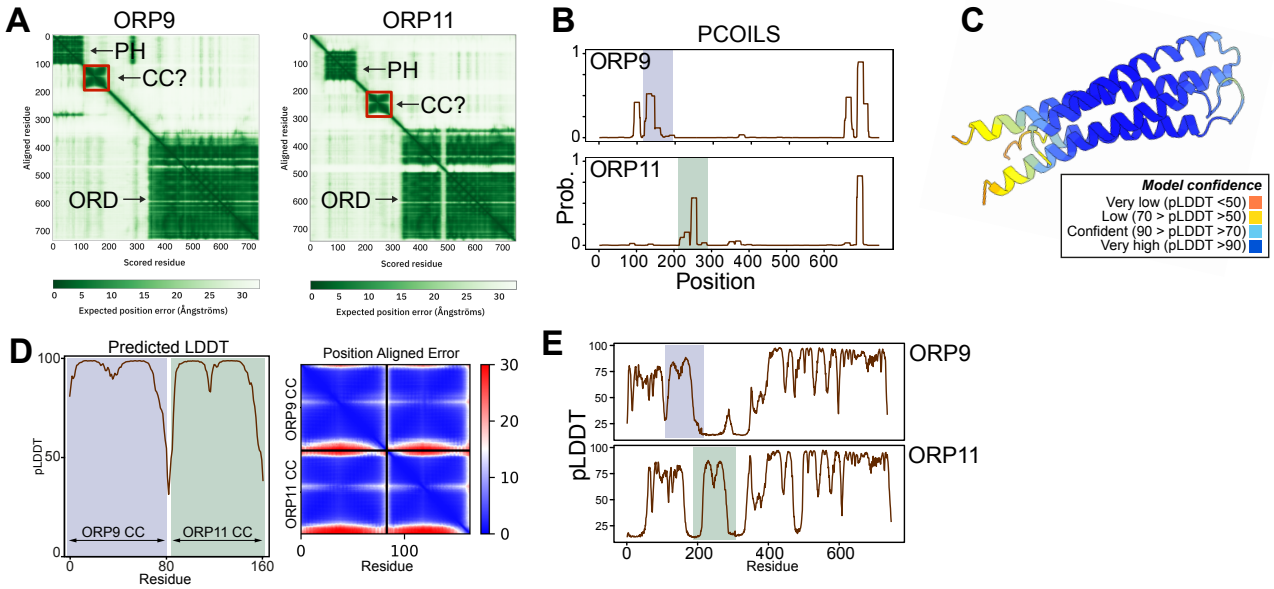


**F**

| *Uniprot* | *Untr* | *BirA* | *VAPA* | *VAPB* | *MOSPD1* | *MOSPD2* | *MOSPD3* |
|---|---|---|---|---|---|---|---|
| OSBL9_HUMAN | 0,0,0 | 0,0,4 | 33,35,50 | 33,26,38 | 0,0,3 | 0,2,3 | 0,0,2 |
| OSB11_HUMAN | 0,0,0 | 4,0,10 | 57,35,55 | 44,25,47 | 3,2,6 | 0,0,4 | 0,0,6 |
| OSBP1_HUMAN | 0,0,0 | 0,0,0 | 15,14,16 | 15,11,7 | 0,0,0 | 0,0,0 | 0,0,0 |

**Supplementary Figure 6: ORP9 and ORP11 interact with each other via their coiled coils.**
(A) AlphaFold prediction of ORP9 and ORP11 reveals secondary structures between their PH and ORD domains. (B) PCOILS predicts coiled coils in the same of both proteins. Residues corresponding to coiled coils are highlighted. (C) AlphaFold-multimer / ColabFold prediction for ORP9-ORP11 coils dimerization. (D) Predicted local distance difference test (pLDDT) and position aligned error plots for panel C. (E) Predicted local distance difference test for figure 4C. (F) Unique peptide counts from BioID experiments performed with VAPA, VAPB, MOSPD1, MOSPD2, and MOSPD3 from Cabukusta *et al*. 2020. Both ORP9 and ORP11, despite latter lacking a FFAT motif, detected in BioID experiments with VAPA and VAPB.

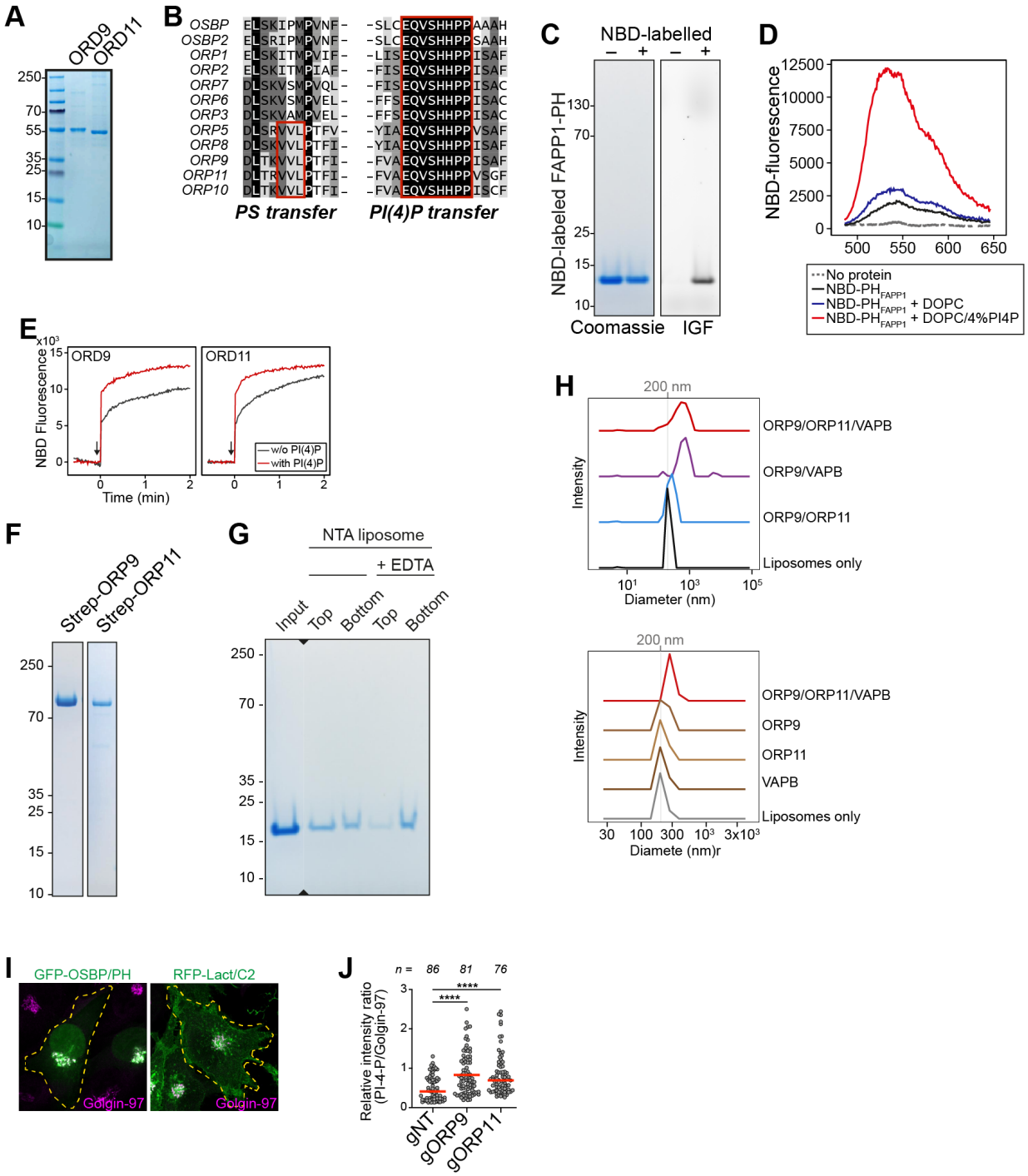


**Supplementary Figure 7: ORP9 and ORP11 are needed for maintaining phospholipid levels in the Golgi.** (A) Coomassie Blue staining of recombinant OSBP-related domains of ORP9 and ORP11. (B) ORP9 and ORP11 contain the critical residues for PS transfer.

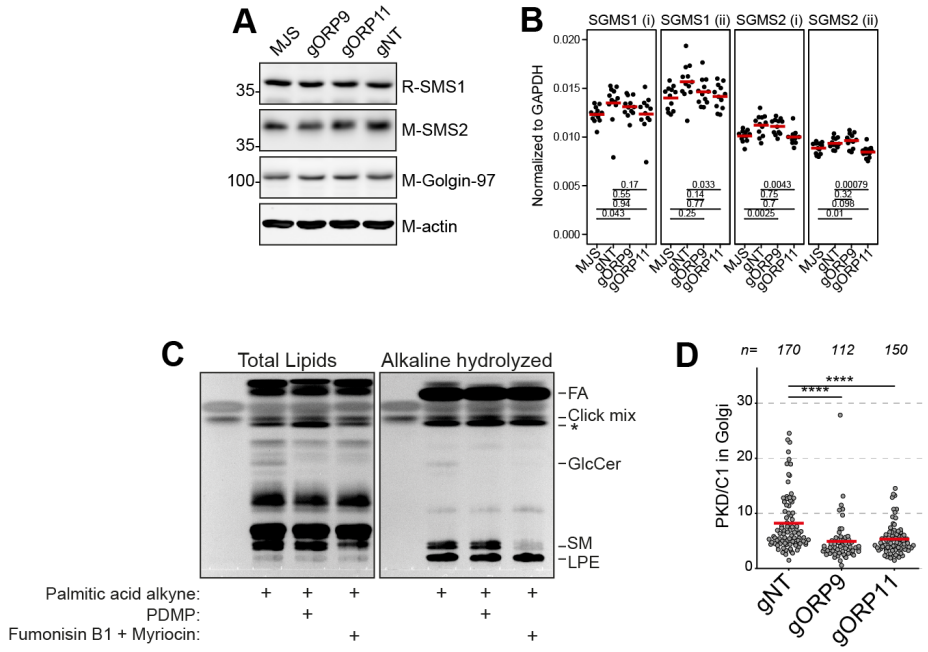


**Supplementary Figure 8: Loss of ORP9 or ORP11 does not affect sphingomyelin synthase levels.** (A) Western blot analysis showing that the protein two human sphingomyelin synthases, SMS1 and SMS2, are not affected in ORP9 and ORP11 knockouts. (B) qRT-PCR showing that mRNA levels of SMS1 and SMS2 are not affected dramatically in knockout cells. Two primer sets per protein each was used (shown with roman numbers). Red lines correspond to mean values. (C) Thin-layer chromatography analysis visualizing the conversion of palmitic acid alkyne to sphingomyelin. To define the band corresponding to sphingomyelin, cells were treated with PDMP or with a cocktail of fumonisin B1 and myriocin prior to alkaline hydrolysis. (D) Golgi quantification of the DAG sensor, mCherry-C1ab, indicates reduced DAG levels in this organelle. Red lines correspond to mean from 3 experiments.

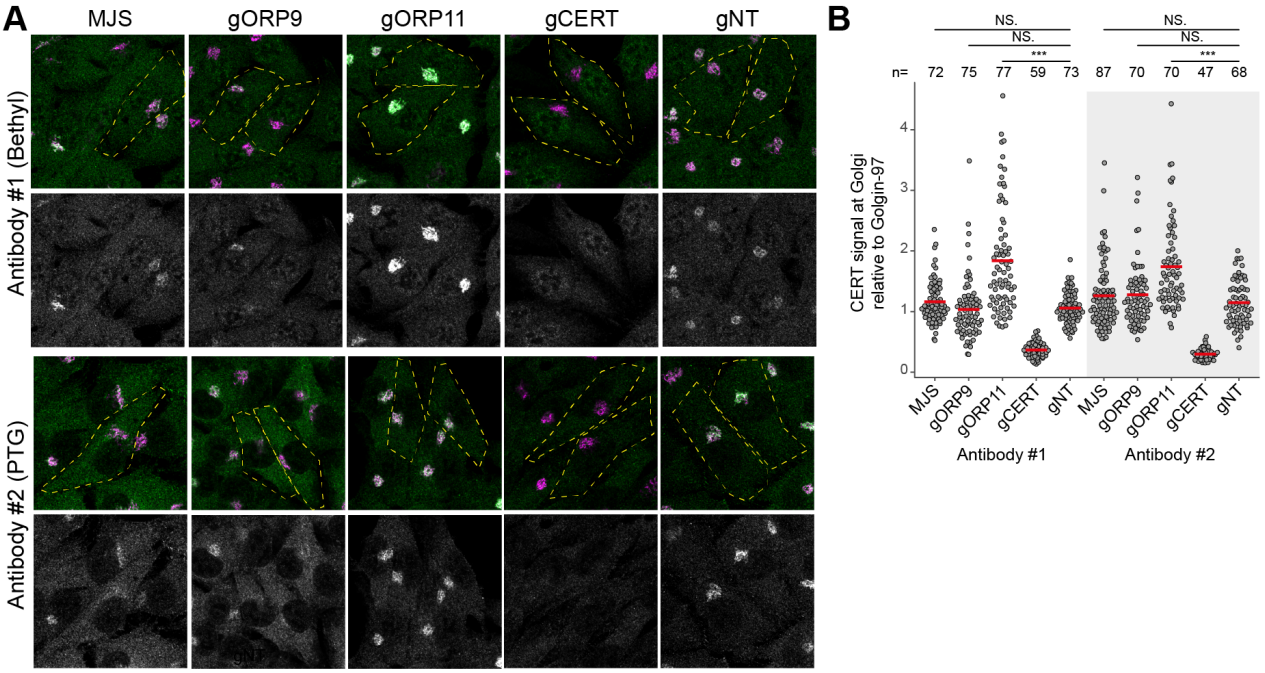


**Supplementary Figure 9: CERT is not less present in the Golgi of ORP9 and ORP11 knockouts.**
(A) Immunofluorescent staining of ORP9, ORP11 and CERT knockout cells using two antibodies against CERT. Note that antibodies fail to stain the Golgi in CERT knockouts. (B) Quantifications corresponding to panel A. Loss of ORP9 or ORP11 do not reduce CERT localization at the Golgi. Note that loss of ORP11 increases CERT localization at the Golgi, shown by two antibodies. Red lines correspond to mean from 3 experiments.

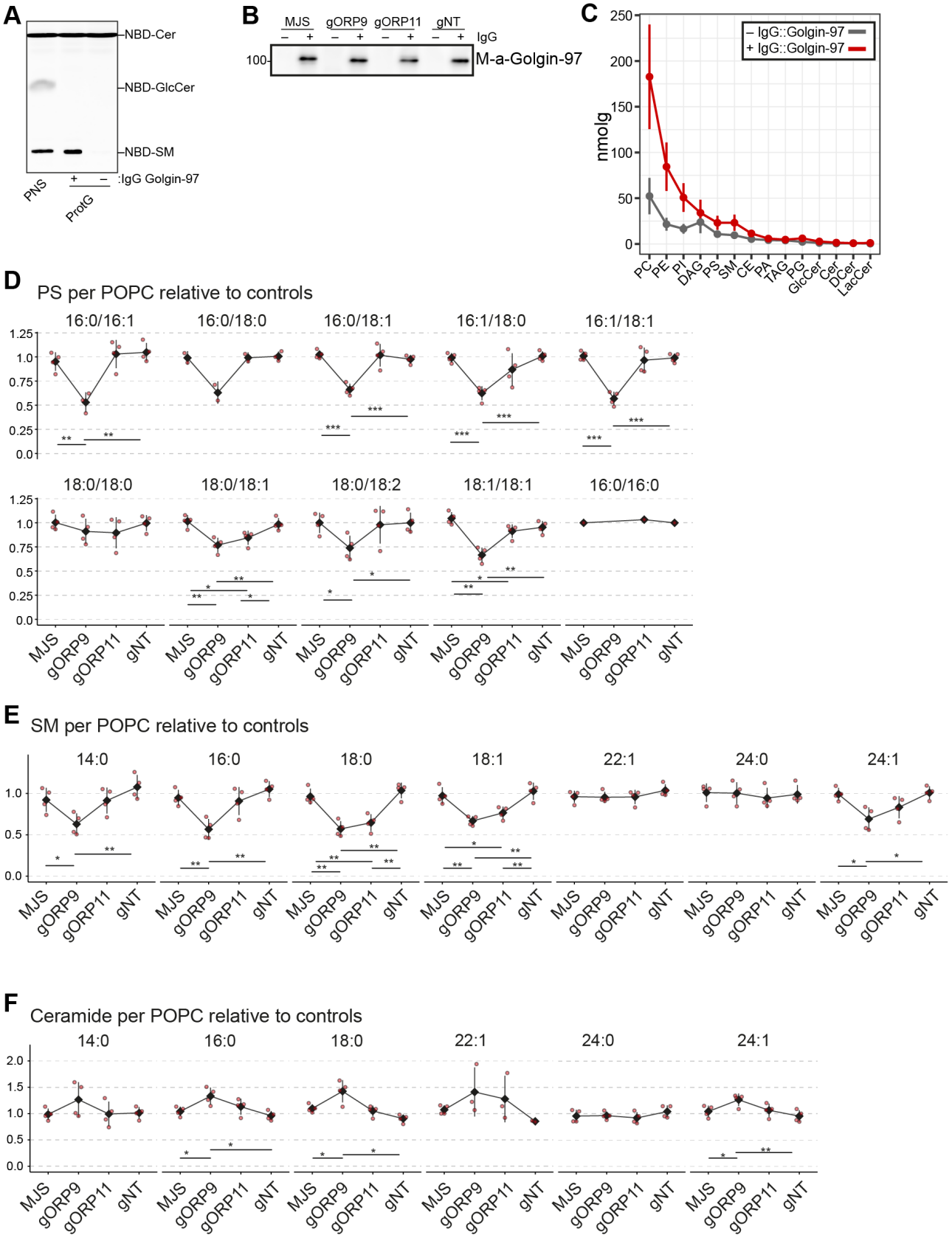


**Supplementary Figure 10: Immunomagnetic isolation yields to intact Golgi membranes.**
(A) Sphingomyelin synthase enzymatic activity assay performed on immunomagnetic Golgi isolates shows that the isolated membranes are intact and enzymatically active. Sphingomyelin synthases contain six transmembrane helices and require intact membrane for activity (Tafesse et al. 2006 “The Multigenic Sphingomyelin Synthase Family” J Biol Chem Volume 281, Issue 40). (B) Western blotting of immunomagnetic

Golgi isolations from knockout cells using Golgin-97 antibody. (C) Amount of lipids isolated from samples in the absence or presence of the *trans* Golgi specific antibody Golgin-97. The plot is based on 16 data points obtained from n=4 experiments. Data points and error bars correspond to mean and standard deviations, respectively. (D) Distribution of PS species. (E) Distribution of sphingomyelin species. (F) Distribution of ceramide species.

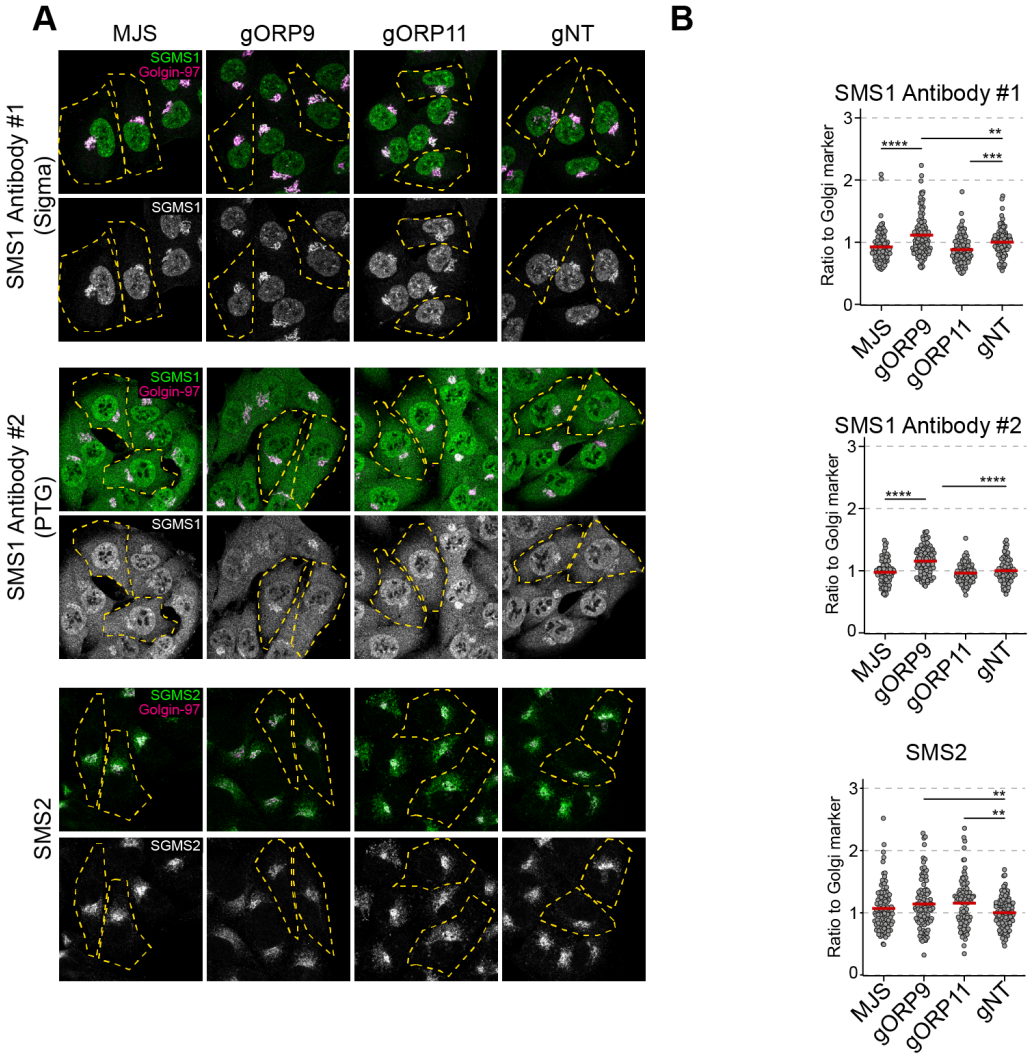


**Supplementary Figure 11: Golgi localization of sphingomyelin synthases is not reduced in ORP9 and ORP11 knockout cells.**

(A) Immunofluorescence images showing localization of sphingomyelin synthases in ORP9 and ORP11 knockout cells. (B) Quantification of images corresponding to panel A. Note that the localization of SMS1 or SMS2 is not reduced in the knockout cells. An increased localization for SMS1 in the Golgi apparatus in ORP9 knockout cells is detected by two antibodies. Red lines correspond to mean from 3 experiments.

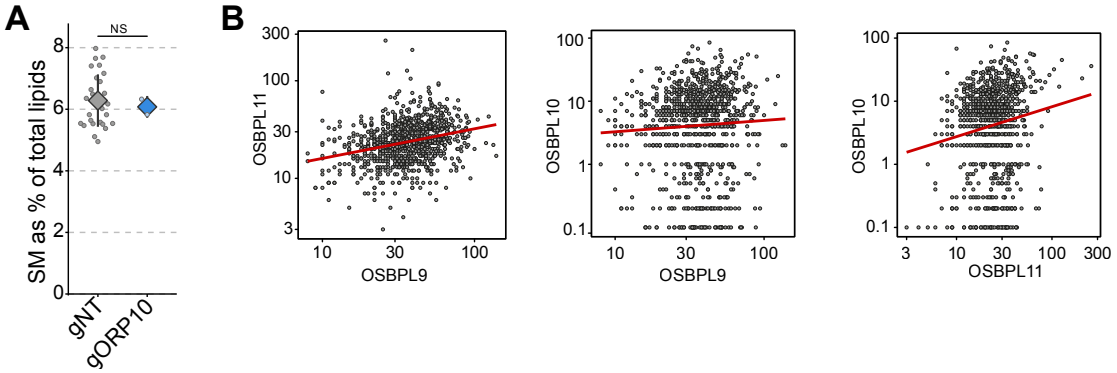


**Supplementary Figure 12: ORP10 knockouts do not display sphingolipid imbalances.**
(A) Lipidomics analysis of ORP10 knockouts do not reveal sphingolipid imbalances that are observed in ORP9 or ORP11 knockouts. (B) Expression analysis from Cancer Cell Line Encyclopedia shows that ORP9, ORP10 and ORP11 are not differentially expressed, but show a positive correlation.